Interpretation of the Observed Neutrino Emission from Three Tidal Disruption Events

Walter Winter[1] and Cecilia Lunardini[2]

[1] Deutsches Elektronen-Synchrotron DESY, Platanenallee 6, D-15738 Zeuthen, Germany
[2] Department of Physics, Arizona State University, 450 E. Tyler Mall, Tempe, AZ 85287-1504 USA; Cecilia.Lunardini@asu.edu

Abstract

Three Tidal Disruption Event candidates (AT2019dsg, AT2019fdr, and AT2019aalc) have been associated with high-energy astrophysical neutrinos in multimessenger follow-ups. In all cases, the neutrino observation occurred $\mathcal{O}(100)$ days after the maximum of the optical-ultraviolet (OUV) luminosity. We discuss unified fully time-dependent interpretations of the neutrino signals where the neutrino delays are not a statistical effect, but rather the consequence of a physical scale of the post-disruption system. Noting that X-ray flares and infrared (IR) dust echoes have been observed in all cases, we consider three models in which quasi-isotropic neutrino emission is due to the interactions of accelerated protons of moderate, medium, and ultra-high energies with X-rays, OUV, and IR photons, respectively. We find that the neutrino time delays can be well described in the X-ray model assuming magnetic confinement of protons in a calorimetric approach if the unobscured X-ray luminosity is roughly constant over time, and in the IR model, where the delay is directly correlated with the time evolution of the echo luminosity (for which a model is developed here). The OUV model exhibits the highest neutrino production efficiency. In all three models, the highest neutrino fluence is predicted for AT2019aalc, due to its high estimated supermassive black hole mass and low redshift. All models result in diffuse neutrino fluxes that are consistent with observations.

Unified Astronomy Thesaurus concepts: Neutrino astronomy (1100); Tidal disruption (1696)

1. Introduction

Nearly a decade after their discovery, the high-energy extragalactic neutrinos seen by IceCube (Aartsen et al. 2013)—possibly indicating the production sites of the Ultra-High Energy Cosmic Rays (UHECRs)—are still largely a mystery, as their origin is still unresolved. Neutrino alert-triggered follow-up searches in electromagnetic data have proven successful to identify individual active galactic nuclei (AGN) blazars as sources; the most prominent case is TXS 0506 + 056, which was found to be in a gamma-ray flaring state during the neutrino emission (Aartsen et al. 2018). In time-integrated point-source searches, individual neutrino sources are also emerging (Aartsen et al. 2020a): three AGN blazars (including TXS 0506+056), and a starburst galaxy (NGC 1068). The most sensitive limits for transient sources exist for the stacking of gamma-ray bursts (Abbasi et al. 2012; Aartsen et al. 2017), which indicate that these can only contribute to the diffuse neutrino flux at the percent level. Arguments from actual neutrino event detections and population statistics (Bartos et al. 2021), as well as from spectral shape and directional information (Palladino & Winter 2018) point toward multiple source populations contributing to the astrophysical diffuse neutrino flux; such populations could be (apart from misidentified atmospheric neutrino events) AGN blazars, AGN cores, starburst galaxies, neutrinos of Galactic origin, and/or tidal disruption events (TDEs).

TDEs are phenomena in which a massive star passes close enough to a supermassive black hole (SMBH) to be ripped apart by its tidal forces. Following this process of tidal disruption, about half of the star's matter remains bound to the

SMBH and is ultimately accreted onto it. Observationally, this mass accretion results in a months- or year-long flare, with the emission of photons over a wide range of wavelengths, including a blackbody (BB) spectrum in the optical-ultraviolet (OUV) range, as well as sometimes X-ray, infrared (IR), and radio emission (see, e.g., Stein et al. 2021b). From observations and numerical modeling, the basic picture of the post-accretion phase of a TDE has emerged, including an accretion disk, a semirelativistic outflow, and possibly a jet (see, e.g., Dai et al. 2018). Neutrinos have been associated with TDEs through follow-up searches; the Zwicky Transient Facility has been especially successful, leading to the identification of AT2019dsg (Stein et al. 2021b) and AT2019fdr (Reusch et al. 2022) as optical counterparts of two neutrinos (IceCube events IC191001A and IC200530A, respectively). Afterwards, it was noticed that these TDEs were accompanied by an echo due to reprocessing of BB and X-ray radiation into the IR by surrounding dust, and this neutrino-dust link then led to the identification of a third TDE, AT2019aalc, as a counterpart of the IceCube event IC191119A (van Velzen et al. 2021a). With three neutrino-TDE associations in less than 1 yr, the case for TDEs as neutrino sources has become stronger,[3] and it is therefore timely to revisit the neutrino production mechanism in TDEs, and the contribution of TDEs to the observed neutrino

---

[3] Note that AT2019fdr and AT2019aalc have not uniquely been identified as TDEs. Alternative interpretations are, e.g., AGN accretion flares or even luminous supernovae (Pitik et al. 2022). All events share TDE-characteristic features, namely the evolution of the BB light curve—including the large and rapid optical flux increase (Reusch et al. 2022)—and the large dust echoes (van Velzen et al. 2021a). Also note that AT2019fdr and AT2019aalc occurred in AGNs (i.e., black holes that were accreting prior to the optical flare). However, the extreme properties of the flares compared to normal AGN variability suggest that the optical outbursts are likely induced by the disruption of a star. Here we adopt the hypothesis that the three objects considered here are indeed TDEs, and therefore will be called as such; the wording "candidates" will be dropped from here on.

diffuse flux at IceCube, which was constrained to be ≲30% in a stacking search (Stein 2020).

Neutrino production in TDEs was proposed earlier in jetted models (Wang et al. 2011; Wang & Liu 2016; Dai & Fang 2017; Lunardini & Winter 2017; Senno et al. 2017), mostly motivated by observations of the jetted TDE Swift J1644 + 57. Furthermore, neutrino production in different disk states (Hayasaki & Yamazaki 2019) and ejecta–external medium interactions (Fang et al. 2020) were considered. TDEs may also be candidates to accelerate and even power the UHECRs (Farrar & Gruzinov 2009; Farrar & Piran 2014; Zhang et al. 2017; Biehl et al. 2018b; Guépin et al. 2018). For AT2019dsg, jets (Liu et al. 2020; Winter & Lunardini 2021), outflow–cloud interactions (Wu et al. 2022), disk, corona, hidden winds, or jets (Murase et al. 2020b) have been proposed (see Hayasaki 2021 for an overview). While a collimated outflow, such as a jet, has the advantage that it can provide the necessary power for the neutrino emission (see discussion in Winter & Lunardini 2022), no convincing direct jet signatures for AT2019dsg have been observed (Mohan et al. 2022), and the observed radio signal might only be interpreted as a jet signature in scenarios with purely leptonic radiative signatures for an unnaturally narrow jet (Cendes et al. 2021) or a steep density profile (Cannizzaro et al. 2021). For AT2019fdr, corona, hidden wind, and jet models have been considered in Reusch et al. (2022), and in van Velzen et al. (2021a), a disk model for all three TDEs has been proposed. The neutrino production site is therefore uncertain, and comparative quantitative studies of all three TDEs do not yet exist.[4]

In this work, we provide a unified quantitative description of the three observed neutrino-emitting TDEs, AT2019dsg, AT2019fdr, and AT2019aalc. We build on the fact that these TDEs have a few common characteristics beyond the detected IR dust echoes: (i) the most likely neutrino energies are in the 100 TeV range, and (ii) the neutrinos arrived $\mathcal{O}(100)$ days after the BB peak—when the BB luminosities have already decreased significantly, but the dust echoes have been close to their maxima. Moreover, (iii) X-rays from all of the neutrino-associated sources have been detected, although X-ray detection is generally rare in TDEs (see, e.g., van Velzen et al. 2021b). In all cases, (iv) the estimated SMBH masses (with large uncertainties) are between about $10^{6.5}$ and $10^{7.5}\, M_\odot$ (van Velzen et al. 2021a), with two of them being higher than the mean of the observed population ($\overline{M} \simeq 10^{6.57}\, M_\odot$; see Nicholl et al. 2022; Ramsden et al. 2022). Consequently, all events should have correspondingly high BB luminosities as a consequence of high Eddington luminosities—for which the measured values in the OUV range are only lower limits, due to obscuration effects.

These commonalities immediately raise important questions: is the neutrino production associated with the X-ray, OUV, or IR signals, i.e., what is the smoking gun signature for the neutrino production? What causes the neutrino time delay with respect to the BB peak, and is that always expected? What can we learn from the predicted neutrino spectra in comparison with the observed neutrino energies? Are the neutrino spectra evolving with time? Some of these questions have been examined in a qualitative way, for example, by suggesting that the neutrino time delay might be directly related to the time evolution of the mass accretion rate, which could be delayed by the debris circularization time, or stay constant over a timescale
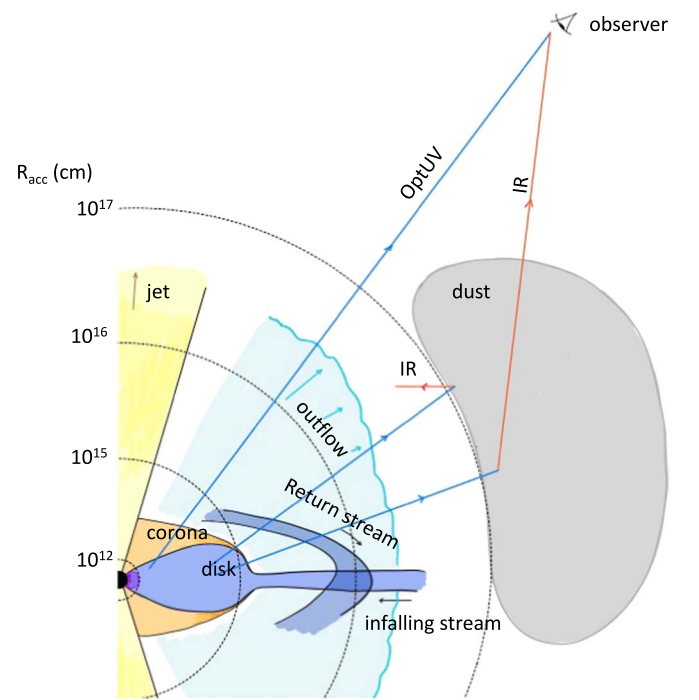
---

[4] After completion of this work, a choked jet model for all three TDEs has been presented in Zheng et al. (2022).

Figure 1. Global geometry of a TDE, illustrated. We show the main elements, some of which may not always be present (e.g., the jet). Three photon histories are sketched, representing the OUV flare, the delayed IR echo, and backwards-emitted IR photons. The dotted circles indicate the several possibilities for the acceleration radius, R_{acc} (the smallest scale, corresponding to the X-ray photosphere inside the accretion disk, is expanded for visibility). A reference SMBH mass $M = 10^7\, M_\odot$ is adopted here.

of hundreds of days (van Velzen et al. 2021a). Here we address these questions by developing a fully quantitative, time-dependent model of neutrino production. We take the point of view that the neutrino time delays have a physical origin—in a characteristic time or length scale of the post-disruption system—instead of being statistical effects. We aim at keeping the models as minimal as possible, by only introducing the strictly necessary ingredients that can be common to different acceleration scenarios. Specific possible accelerators and their feasibility will be discussed briefly for context.

Our study is organized as follows: in Section 2 we introduce the model and describe its details. Results are presented for three realizations (named M-X, M-OUV, and M-IR, after the three different photon targets used), in Sections 3, 4, and 5, respectively. We present our results for the diffuse fluxes in Section 6, and we compare the different TDEs and models in Section 7. We finally summarize in Section 8. Three technical Appendices A–C are included at the end of the paper.

2. Model Description

In this section, we describe the spirit and the ingredients of our model. For a reader wanting a quick overview, Section 2.1, Figure 1, and Table 1 summarize the qualitative features and numbers. Our method to describe the dust echo is presented in Section 2.5.

2.1. Overview

To explain the emission of high-energy neutrinos, protons must be accelerated to energies beyond ∼PeV, and interact with background photons and/or matter. The neutrinos are then

Table 1
Summary of Observations and Universal Model Ingredients

	AT2019dsg	AT2019fdr	AT2019aalc
Overall Parameters			
Redshift z	0.051 (1)	0.267 (2)	0.036 (3)
t_{peak} (MJD)	58603 (4)	58675 (2)[a]	58658 (3)
SMBH mass M [$M_\odot$]	5.0 10^6 (3)	1.3 10^7 (3)	1.6 10^7 (3)
Neutrino Observations			
Name (includes t_ν)	IC191001A (5)	IC200530A (6)	IC191119A (7)
$t_\nu - t_{peak}$ [days]	154	324	148
E_ν [TeV]	217 (5)	82 (6)	176 (7)
N_ν (expected, GFU)	0.008–0.76 (1)	0.007–0.13 (2)	not available
BB (OUV)			
T_{BB} [eV] at t_{peak}	3.4 (1)	1.2 (2)	0.9 [Section 2.5]
L_{BB}^{bol} (min.) [$\frac{erg}{s}$] at t_{peak}	2.8 10^{44} (Section 2.5)	1.4 10^{45} (Section 2.5)	2.7 10^{44} (Section 2.5)
BB evolution from	(1)	(2)	(3)
X-Rays (X)			
T_X [eV]	72 (1)	56 (2,3)	172 (3)
L_X^{bol} [$\frac{erg}{s}$] @ $t - t_{peak}$	6.2 10^{43} @ 17 days (1)	6.4 10^{43} @ 609 days (2)	1.6 10^{42} @ 495 days (3)
Dust Echo (IR)			
T_{IR} [eV]	0.16 (Section 2.5)	0.15 (2)	0.16 (Section 2.5)
Time delay Δt [days]	239 (Section 2.5)	155 (Section 2.5)	78 (Section 2.5)
L_{IR}^{bol} [$\frac{erg}{s}$] @ $t - t_{peak}$	2.8 10^{43} @ 431 days (Section 2.5)	5.2 10^{44} @ 277 days (Section 2.5)	1.1 10^{44} @ 123 days (Section 2.5)
Universal Model Assumptions—and Their Consequences			
ε_{diss} ($L_p/\dot{M}$)	0.05–0.2	0.05–0.2	0.05–0.2
F_{peak} ($\dot{M}/L_{edd}$ at t_{peak})	100	100	100
$M_\star/M_\odot$ ($M_\star \simeq 2 \cdot \int \dot{M} dt$)	0.6	5.7	6.3
t_{dyn} [days] (interval with $\dot{M} \gtrsim L_{edd}$)	670	1730	1970

Note. The X-ray and IR luminosities are given at the indicated times, with the evolution determined by our theoretical models (for details, see the main text). The neutrino time delay $t_\nu - t_{peak}$ is computed from t_{peak} and t_ν. See caption of Figure 4 for the definition of the GFU (gamma-ray follow-up) effective area.
[a] Peak position uncertain; here a value close to epoch 1 of the BB peak in (2) is chosen.
References to the original articles or Sections in this article are given as well in Brackets: (1) Stein et al. (2021b), (2) Reusch et al. (2022), (3) van Velzen et al. (2021a), (4) van Velzen et al. (2021b), (5) IceCube Collaboration (2019a), (6) IceCube Collaboration (2020), (7) IceCube Collaboration (2019b).

natural results of these interactions. In the spirit of minimality, we assume that the nonthermal proton injection: (i) is (quasi-)isotropic (rather than beamed as in jetted models), and (ii) evolves in time, like the mass accretion rate. The latter assumption seems contrary to the idea of reproducing the neutrino time delays, because it naturally leads to a neutrino signal that follows the BB luminosity evolution. Still, within this basic scenario, there are multiple ways to reproduce the

neutrino delays, since these can be related to other important time or length scales of the post-disruption system.

Elaborating on the latter point, let us examine the large-scale structure of a TDE after the disruption has occurred, as shown in Figure 1. In the figure, the components where proton acceleration could take place, and their characteristic radial scales, are illustrated for a reference SMBH mass $M = 10^7 M_\odot$ (gravitational radius $R_S \simeq 3 \cdot 10^{12}$ cm). The figure illustrates how the location of the proton acceleration (radial distance $R = R_{acc}$) can vary widely, from $R_{acc} \sim (3 - 30) R_S$ (the X-ray photosphere and the hot corona; see, e.g., Murase et al. 2020b and discussion in van Velzen et al. 2021a), to $R_{acc} \sim 10^3 R_S$ (the OUV photosphere, or the collision region inside a jet; see, e.g., Dai et al. 2018) or even larger values like $R_{acc} \sim 10^{16}$–10^{17} cm, for acceleration inside the outflow (possibly near the dust torus; Stein et al. 2021b), or in stream-stream collisions (Dai et al. 2015; Hayasaki & Yamazaki 2019). Which of these possibilities are consistent with our models will be examined later (see Sections 3, 4, and 5). In some cases, the neutrino delay might be reproduced by a geometric distance; for example, higher-energy protons could interact with the IR photons from the dust echo, which carries a delay from the size of the dust region. In other cases, the delay might arise from the dynamics of proton propagation: e.g., lower-energy protons—such as those leaking out of an off-axis jet (see Appendix A for a discussion)—could be confined in magnetic fields over the diffusion time, and transfer energy into secondaries in the calorimetric limit. For generality, here we do not specify the *proton acceleration zone* in detail, but rather characterize it by the maximal proton energy achieved, $E_{p,max}$ (equivalent to the maximal Lorentz factor), and the proton injection luminosity and its evolution, similarly to AGN blazar radiation models (see, e.g., Keivani et al. 2018; Gao et al. 2019; Oikonomou 2022). For a discussion on realistic proton energies that can be achieved if the acceleration and radiative processes are considered, as well as other constraints (for shock acceleration, the shocks ought not be radiation-mediated); see Appendix C. We focus instead on the *radiation zone*, i.e., the region at $R \gtrsim R_{acc}$ where the neutrinos are produced.

We start by observing that the preferred photon target depends on the maximal proton energy provided by the accelerator. Indeed, for $p\gamma$ interactions, the observed neutrino energies in the 100 TeV range indicate BB target photon temperatures[5]

$$T \simeq 80 \text{ eV} \left(\frac{E_\nu}{100 \text{ TeV}} \right)^{-1}, \quad (1)$$

in the (soft) X-ray range. Since, however, depending on the spectral shape the actual neutrino energies may be significantly higher for observed muon tracks, lower target photon temperatures in the OUV or IR ranges paired with neutrinos peaking at higher energies may work as well, provided that the accelerator is efficient enough. Using Equation (1), the requirement

$$E_{p,max} \gtrsim 20 E_\nu \simeq 160 \text{ PeV} \left(\frac{T}{\text{eV}} \right)^{-1} \quad (2)$$

---

[5] In this estimate, both the pitch-angle averaged cross section (see Figure 4 in Hummer et al. 2010) and the peak of the photon number density located at $\simeq 2.8 \, T$ (Fiorillo et al. 2021) are taken into account.

translates then into $E_{p,\mathrm{max}} \gtrsim 2\,\mathrm{PeV}$, $E_{p,\mathrm{max}} \gtrsim 100\,\mathrm{PeV}$, and $E_{p,\mathrm{max}} \gtrsim 1\,\mathrm{EeV}$ for X-rays, OUV, and IR targets, respectively. Detailed parameters for the individual TDE electromagnetic spectra are listed in Table 1. We will study these options systematically, increasing $E_{p,\mathrm{max}}$ within three models called M-X, M-OUV, and M-IR, making additional target photon fields accessible for the interactions. In some cases, pp interactions with the outflow will also contribute significantly, especially if no high target photon densities are accessible.

Note that our model assumptions will be as universal as possible, which means that common parameters are chosen for all TDEs if physically motivated. This assumption simplifies the comparison, whereas the very different redshifts of the TDE candidates with associated neutrinos jeopardize the direct comparison of neutrino fluences or event rates; see Table 1. In fact, we will see that the predicted neutrino emission is not as different as one might expect if the neutrino luminosity or spectra (at the source) are compared.

Compared to other models in the literature, our model M-X shares some similarities with the hidden wind model in Murase et al. (2020b), and our model M-OUV is in fact a time-dependent numerical implementation of the idea proposed in Stein et al. (2021b). Our model M-IR is motivated by the dust echo connection of the neutrino-emitting TDEs (van Velzen et al. 2021a), postulating a direct connection. Therefore, we develop our own dust model to obtain the time-dependent luminosity of the IR echo (see Section 2.5). Compared to jetted models, the main challenge for the presented models (and in fact most quasi-isotropic emission models) are the very high required transfer efficiencies of material of the disrupted star into nonthermal protons. This problem can be avoided in models with a collimated outflow; see discussion in Winter & Lunardini (2022). However, the difference between isotropic and collimated emission models is more fundamental: are TDEs inefficient neutrino emitters each with the contribution of a fraction of an event on average, invoking the Eddington bias argument (Strotjohann et al. 2019), or are they more efficient neutrino emitters perhaps just not pointing into our direction, or are they too far away in most cases? Since we focus on the isotropic case in this study, the predicted neutrino event number per TDE will be an interesting indicator if the Eddington bias argument has to be invoked for each individual TDE.

In the following subsections, we describe the elements that are common to all of the models, whereas specifics will be discussed in the following respective results sections.

2.2. Numerical Time-dependent Simulation of Radiation Zone

We solve the coupled differential equation system for the in-source densities N_i (differential in energy and volume)

$$\frac{\partial N_i(E,t)}{\partial t} = \underbrace{\tilde{J}_i(E,t)}_{\mathrm{Injection}} + \underbrace{\frac{\partial}{\partial E}\left(\frac{E}{t_{\mathrm{cool}}(E,t)}N_i(E,t)\right)}_{\mathrm{Cooling}}$$
$$- \underbrace{\frac{N_i(E,t)}{t_{\mathrm{esc}}(E,t)}}_{\mathrm{Escape}} \qquad (3)$$

for the protons ($i = p$) and neutrons ($i = n$) in a fully time-dependent way using the NeuCosmA software (Hummer et al. 2010, 2012; Boncioli et al. 2017; Biehl et al. 2018a). Here the

cooling rate is given by $t_{\mathrm{cool}}^{-1} = E^{-1}|dE/dt|$, the escape rate by t_{esc}^{-1}, and the injection rate $\tilde{J}_p(E) = J_p(E) + J_{j\to p}(E)$ (differential in volume, energy and time) contains the injection from the acceleration zone J_p as well as the re-injection $J_{j\to p}$ from interacting protons at higher energies and interacting neutrons ($j = p$, n)—which couples the differential equations; for neutrons, corresponding terms are used, but there is no injection from an acceleration zone, i.e., $J_n(E) \equiv 0$.

Photohadronic interactions are treated as discrete energy losses as described in Biehl et al. (2018a), which means that escape terms with the interaction rate $t_{p\gamma}^{-1}$ are added and the interaction products are re-injected in $J_{j\to p}$ at lower energies; we use the efficient but accurate treatment of Biehl et al. (2018a) and Hummer et al. (2010) based on the physics of SOPHIA (Mucke et al. 2000). The emitted neutrinos are integrated over time, while the in-source densities N_i are evolved over the lifetime of the system (as shown in our figures). Since the proton injection rate varies with time, a steady state will never be reached. Protons also cool via Bethe–Heitler pair production; note that all of these injection, escape, and cooling rates are explicitly time-dependent through the time-dependent evolution of the target photon fields.

Protons escape diffusively, see below, or by interactions, whereas neutrons escape over the free-streaming timescale $t_{\mathrm{fs}} \simeq R/c$. We also assume that protons escape over the duration of the TDE, referred to as dynamical timescale t_{dyn} here (see Section 2.3 for its definition as one possible measure for the duration of the TDE event) to take into account the transient nature of the event; however, the impact of that term on the neutrino production is small. We also include synchrotron losses for all charged species (including the secondary muons, pions, and kaons).[6]

Our approach can properly treat the optically thick case (see App. C of Biehl et al. 2018a), which we define as $\tau_{p\gamma}^{\mathrm{fs}} \equiv t_{\mathrm{fs}}/t_{p\gamma} > 1$ (protons interact efficiently while crossing the radiation zone), and the calorimetric case, which we define as $\tau_{p\gamma}^{\mathrm{cal}} \equiv t_{\mathrm{dyn}}/t_{p\gamma} > 1$ (magnetically confined protons interact efficiently over the duration of the system, even if $\tau_{p\gamma}^{\mathrm{fs}} < 1$). We will find the calorimetric case for interactions in model M-X, where the proton energies are low, and the optically thick case for M-OUV, where the interaction rates are high (M-IR is in between). Note that the effective photohadronic cooling rate $t_{p\gamma,\mathrm{cool}}^{-1} \simeq 0.2\, t_{p\gamma}^{-1}$ does not apply to the (optically thin) calorimetric case, since neutrons produced in the interactions can escape over the free-streaming timescale, and hence the effective cooling rate will be much higher; consequently, we only show interaction rates where applicable, while our numerical treatment reproduces all of these effects self-consistently. Furthermore, note that the calorimetric approach requires that adiabatic cooling be sufficiently small, which depends on the expansion of the radiation zone: if (magnetically confined) protons lose energy faster than they can interact, the adiabatic cooling will affect the production rate of neutrinos especially for model M-X; see discussion in Appendix B.

---

[6] For the neutrino flavor composition, the effects are negligible because of very high critical energies due to the relatively small values of B; see, e.g., Appendix A.1 of Baerwald et al. (2012).

2.3. Energetics, Proton Injection, and Proton Confinement

The Eddington luminosity $L_{edd} \simeq 1.26\ 10^{45}(M/(10^7\ M_\odot))$ erg s^{-1}—where M is the SMBH mass—is a measure for the energy reprocessing rate through the SMBH, where super-Eddington mass accretion rates are expected for TDEs at peak; we use the inferred SMBH masses listed in Table 1. Following Dai et al. (2018), we assume that the mass accretion rate $\dot{M}$ exceeds L_{edd} by a factor $F_{peak} \simeq 100$ at peak. While the mass fallback rate is expected to scale $\propto t^{-5/3}$ generically, we more accurately implement that the mass accretion rate roughly follows the observed BB evolution for each individual TDE; for details and references, see Table 1.

We parameterize the proton injection spectrum J_p (density differential in energy and time) as

$$J_p = J_0\ E_p^{-2} \exp\left(-\frac{E_p}{E_{p,max}}\right), \qquad (4)$$

where $E_{p,max}$ is a parameter depending on the model (M-X, M-OUV, or M-IR). The nonthermal proton injection luminosity L_p is dynamically following the mass accretion rate $\dot{M}$, and is given by

$$L_p = \varepsilon_{diss}\ \dot{M}\ c^2 = \varepsilon_{Comp}\ \varepsilon_{NT}\ \dot{M}\ c^2. \qquad (5)$$

Here $\varepsilon_{diss} \equiv \varepsilon_{Comp}\ \varepsilon_{NT}$ is the dissipation efficiency, which we define as the fraction of the accretion luminosity, $\dot{M}\ c^2$, which is converted into nonthermal particles (which are dominated by protons in our models). It contains the conversion efficiency, ε_{Comp}, from the infalling material into a component, such as an outflow, corona, or jet; for example, in the TDE unified model (Dai et al. 2018), $\varepsilon_{Comp} \simeq 0.2$ for outflow or jet. It also contains the dissipation efficiency of kinetic power into nonthermal particles, ε_{NT}. For the outflow and wind models, one may estimate that $\varepsilon_{NT} \sim v^2/c^2$, whereas for jetted internal shock models (see, e.g., Equation (10) in Daigne & Mochkovitch 1998 or Equation (4) in Rudolph et al. 2020 for the definition of ε_{NT} in this case), one finds a wide range $\varepsilon_{NT} \sim 0.1$–$0.4$ (see Appendix A). We need to postulate relatively high overall dissipation efficiencies, $\varepsilon_{diss} \simeq 0.05 - 0.2$, into nonthermal protons, where $\varepsilon_{diss} \simeq 0.2$ represents an optimistic choice with $\varepsilon_{NT} \sim 1$, and $\varepsilon_{diss} \simeq 0.05$ corresponds to an outflow with $v = 0.5\ c$ (in the direction of the poles, where the particle acceleration will be most efficient; see Dai et al. 2018) or a jet with $\varepsilon_{NT} \simeq 0.25$. We therefore show the results for the range $\varepsilon_{diss} \simeq 0.05 - 0.2$, where applicable. Note that, as we will demonstrate, a high value of ε_{diss} can be also viewed as a requirement to produce a neutrino fluence compatible with the expected average neutrino event rate derived from observations (see Table 1), as the predicted neutrino event rate is proportional to ε_{diss}. On the other hand, there are factors that may relax this requirement: we use 1 GeV as lower energy of the nonthermal proton spectrum, as we anticipate that the protons are picked up from a thermal bath. This assumption for the minimal proton energy is conservative, as a lot of energy will be transferred into nonthermal protons that are below the $p\gamma$ threshold; it may result in a reduction of ε_{diss} by up to a factor of 5 if the minimal proton injection energy is higher. Furthermore, note that TDEs that occurred in an AGN—such

as AT2019fdr and AT2019aalc–may draw material from the existing disk as, in general, TDEs in AGNs seem to be more luminous (see, e.g., Chan et al. 2021). This would also lower the requirement for the dissipation efficiency for a fixed mass of the disrupted star.

The proton spectrum normalization J_0 in the radiation zone is obtained from the proton luminosity L_p

$$\int_{1\ GeV}^{\infty} dE_p\ E_p\ J_p(E_p) = \frac{L_p}{\frac{4}{3}\ R^3\ \pi}. \qquad (6)$$

We note that the relation between the size of the radiation zone R and the acceleration location $R_{acc} \lesssim R$ depends on the model (see Sections 3–5).

Another measure for the available energy is the mass of the disrupted star. Since about half of the stellar debris accreted toward the SMBH, we can estimate the mass of the disrupted star as $M_\star \simeq 2 \cdot \int \dot{M} dt$, which we list in terms of solar masses ($M_\odot \simeq 1.8\ 10^{54}$ erg) as a result of our computation in Table 1.[7]

Let us now introduce other fundamental ingredients of our models. One of them is the dynamical timescale t_{dyn} of the TDE, which is roughly estimated as the time period for which $\dot{M} > L_{edd}$. This a suitable definition, since qualitative changes are expected to occur when $\dot{M}$ becomes sub-Eddington, $\dot{M} \ll L_{edd}$ (e.g., transition of the disk accretion state or jet cessation). In practice, the values of t_{dyn} are determined numerically by imposing the condition $\dot{M} > L_{edd}$ on curves that are derived from the BB light curves, assuming that $\dot{M}$ evolves like the BB luminosities.[8]

If the magnetic field in the radiation zone is given by B, protons gyrate with the Larmor radius

$$R_L \simeq 3.3\ 10^{12}\ cm\left(\frac{E_p}{PeV}\right)\left(\frac{B}{G}\right)^{-1}. \qquad (7)$$

Note that the confinement condition $R_{acc} > R_L$ can impose constraints on the size of the accelerator for high enough proton energies; for example, $R_{acc} \gtrsim 3\ 10^{16}$ cm for $E_{p,max} \simeq 1$ EeV and $B = 0.1$ G (see model M-IR). Assuming Bohm-like diffusion with a diffusion coefficient $D \simeq R_L\ c$, protons can be displaced by

$$R \simeq \sqrt{D\ t_{p,diff}} = 3\ 10^{15}\ cm\left(\frac{E_p}{PeV}\right)^{1/2}$$
$$\times \left(\frac{B}{G}\right)^{-1/2}\left(\frac{t_{dyn}}{1000\ days}\right)^{1/2}, \qquad (8)$$

where the diffusion time is set to the dynamical time $t_{p,diff} \simeq t_{dyn}$, and Equation (7) has been used for D. This means

---

[7] Integration ranges in time will correspond to the ranges shown in our figures, e.g., Figure 4, upper row. If material from the preexisting AGN is accreted, half of the reported $M_\star$ correspond to the accreted mass.

[8] To visualize this exercise, see, e.g., Figure 4, where the curves (thick green in upper panels) for $L_p \sim 0.2\ \dot{M}$ (for $\varepsilon_{diss} = 0.2$) and L_{edd} are shown: t_{dyn} corresponds to the time window during that $\dot{M} \simeq 5\ L_p > L_{edd}$. As can also be seen from the figures, we resorted to extrapolating the actual light curves due to lack of data covering the entire time period. We stress that precise values of t_{dyn} do not influence our results much, but are useful as one possible measure for the duration of the TDE. They are of the order 1000 days, with some dependence on the individual TDE.

that protons with PeV energies will be magnetically confined by Gauss-scale magnetic fields in a region of size $R \simeq 3\,10^{15}$ cm over the lifetime of the TDE, and the system will be calorimetric if $t_{p\gamma} < t_{\rm dyn}$ (see, e.g., model M-X). Since the Larmor radius in Equation (7) is for our parameters considerably smaller than the region R, only protons with very high energies can escape directly (ballistically), and protons with $E_p \sim 1$–10 PeV (relevant for the X-ray interactions) are confined. Here we follow Baerwald et al. (2013) and define a self-consistent escape rate for the protons given by

$$t_{p,\rm esc}^{-1} = \min(t_{\rm fs}^{-1}, t_{p,\rm diff}^{-1}) \qquad \text{with} \qquad t_{p,\rm diff}^{-1} \equiv \frac{D}{(c\,t_{\rm fs})^2}, \quad (9)$$

which implies that the diffusive escape rate is limited by the free-streaming rate.[9] Note that magnetic confinement in turbulent magnetic fields also leads to isotropization of the proton-photon pitch angles (the angles between incoming protons and photons in the interaction frame), if not already isotropized.

Finally we discuss the choice of Gauss-scale magnetic fields over such a large region R. Dai et al. (2018) obtained a magnetic flux $\simeq 10^{31}$ G cm^2 at about $80\,R_S$, which translates to about 1 Gauss in a distance of 10^{15} cm. Stein et al. (2021b; see also Stein 2021a) obtained a field of about $B \simeq 0.07$ G from the radio equipartition analysis at $R \simeq 7\,10^{16}$ cm for a radio epoch that was near-contemporaneous to the neutrino detection. Assuming that the field $B \propto 1/R$ for a toroidal configuration, Gauss-scale fields at 10^{15} cm are plausible. In the hidden wind model, Gauss-scale magnetic fields are estimated from the kinetic wind luminosity as well (Murase et al. 2020b; Reusch et al. 2022); in fact, up to 30 G are obtained for AT2019fdr. We obtain similarly large values for our models if the plain equipartition argument is applied to the BB luminosity. Note, however, that the equipartition argument can only be directly applied if the (related) radiation is generated from electromagnetic processes dominated by these B-fields, such as synchrotron emission in the fast-cooling regime. Here the observed thermal spectra are not related to such processes (compared to, e.g., radio emission from an outflow). Since it is crucial for our calorimetric (confinement) models that the magnetic field is high enough (i.e., higher magnetic fields help the confinement), we chose the Gauss-scale as a conservative value that meets the confinement requirement. Higher values for the magnetic field would lead to qualitatively similar results.

2.4. Photon and Proton Targets

Protons encounter target photons and protons within the radiation zone of radius R. All photon targets are described by quasi-thermal spectra with temperature T, motivated by observations. As a short summary, for X-rays, which stem from the accretion disk, we hypothesize that the (highest) detected X-ray flux is indicative for the actually emitted X-ray flux, and obscuration, such as from a complicated geometry or outflow, leads to flux fluctuations—whereas the intrinsic flux within R is relatively stable (see, e.g., Wen et al. 2020). For OUV, we take the BB evolution from observations directly, but

we correct for absorption by inferring the unabsorbed luminosity from the dust echo; see Section 2.5. For IR, we model the dust echo both in terms of time dependence and normalization, as described in the same subsection. More details will also be given in the respective model sections later. The in-source photon density $n(\varepsilon)$ (typically units [GeV^{-1} cm^{-3}]) is then computed from the luminosity L as

$$\int d\varepsilon\,\varepsilon\,n(\varepsilon) = \frac{L\,\tau}{4\,\pi\,R^2\,c}, \qquad (10)$$

were τ is the photon optical thickness approximated by $\tau \sim 1$ (and the implied effective escape time is $t_{\rm esc} \equiv \tau \cdot R/(3\,c)$). This is a good estimate for X-rays ($\tau \simeq 1$), a lower limit estimate for the OUV BB if $R < R_{\rm BB}$ ($\tau > 1$) and a better estimate if $R \gtrsim R_{\rm BB}$ ($\tau \simeq 1$), and a rough estimate for the IR target if R corresponds to the scale of the dust scattering.

We also consider pp interactions with a mildly relativistic outflow because the outflow is a plausible model ingredient, as it may be the reason for the X-ray obscuration. Moreover, the outflow is expected in numerical simulations (e.g., Dai et al. 2018), and it has been directly observed for AT2019dsg (Stein et al. 2021b). Note that there may be interactions of other components, such as debris, clumps or clouds as well, which we however do not describe in view of major geometric and density uncertainties.

As shown in Dai et al. (2018), the outflow densities are high up to about 1000 gravitational radii, which is about 10^{15} cm for $M \simeq 10^7\,M_\odot$ in consistency with Equation (8); therefore, even calorimetric effects may be expected. The relevant target density is computed by assuming that a fraction $\varepsilon_{\rm Outflow} \simeq 0.2$ of the mass accretion is re-processed into the outflow so that $L_{\rm outflow}(t) = \varepsilon_{\rm outflow}\,\dot{M}(t)$ (scaling with the mass accretion rate; Dai et al. 2018). Since $M_{\rm outflow} \simeq L_{\rm outflow}\,\frac{c}{v}\,t_{\rm fs}$ in the production volume, smaller velocities imply higher densities. The free-streaming optical thickness can be estimated as[10]

$$\tau_{pp}^{\rm fs} \equiv \frac{t_{\rm fs}}{t_{pp}} \simeq 0.01 \left(\frac{M}{10^7\,M_\odot}\right)\left(\frac{R}{10^{15}\,\rm cm}\right)^{-1}\left(\frac{v}{0.5\,c}\right)^{-1}, \quad (11)$$

where v is the velocity of the outflow. A comparison to Dai et al. (2018) reveals that $v \simeq 0.5\,c$ near the funnel, whereas $v \simeq 0.1\,c$ perpendicular to that—where the densities are higher. We conservatively use $v \simeq 0.5\,c$. We will see that pp interactions can be important if the X-ray luminosity is low, or at low energies (below the $p\gamma$ threshold). Especially in the calorimetric case, the system can be optically thick for pp interactions as well:

$$\tau_{pp}^{\rm cal} \equiv \frac{t_{\rm dyn}}{t_{pp}} \simeq 19 \left(\frac{M}{10^7\,M_\odot}\right)\left(\frac{R}{10^{15}\,\rm cm}\right)^{-2}$$
$$\times \left(\frac{v}{0.5\,c}\right)^{-1}\left(\frac{t_{\rm dyn}}{600\,\rm days}\right). \qquad (12)$$

---

[9] This definition mimics the transition between the diffusive and free-streaming escape regimes for magnetic field turbulence coherence lengths $l_c \sim R$; see discussion in Becker Tjus et al. (2022).

[10] For this estimate, we use $t_{pp}^{-1} \simeq \sigma_{pp}\,n_H\,c$, where n_H is the target density and $\sigma_{pp} \simeq 60$ mbarn is the cross section for $E_p \simeq 1$ PeV (Kelner et al. 2006). In our numerical approach, the full energy dependence of the cross section is taken into account, following Kelner et al. (2006).

2.5. Dust Echo and Inferred Bolometric Luminosities

For each TDE, an IR light curve was measured at several times after the peak by neoWISE in the W1 and W2 frequency bands. It has been interpreted as thermal emission from a dust torus, which is illuminated and heated by the OUV and X-ray radiation emitted by the TDE accretion disk (see, e.g., van Velzen et al. 2021a). The main features of this IR dust echo are: (i) the delayed emission with respect to the primary OUV and X-ray emission, due to the dust being at an angle with respect to line of sight (see Figure 1); and (ii) a thermal IR spectrum with temperature at or below the dust sublimation temperature of $T_{IR} \simeq 0.16$ eV ($\simeq 1850$ K; van Velzen et al. 2021a; Reusch et al. 2022; see also van Velzen et al. 2016 for a general description of dust properties in TDEs). We use this value unless T_{IR} has been measured; see Table 1.

Assuming that the contribution of the X-rays to the dust echo is negligible in the present case, the energy emitted in IR in the neoWISE bands can be expressed as:

$$E_{IR} = \epsilon_{bol}^{IR} \, \epsilon_{\Omega} \, \epsilon_{dust} E_{BB}^{bol}. \tag{13}$$

Here E_{BB}^{bol} is the total (bolometric) energy in the OUV spectrum, ϵ_{bol}^{IR} is a correction factor describing the ratio between the neoWISE measured luminosity and the bolometric luminosity, $\epsilon_{\Omega} = \Omega/4\pi$ is the geometric covering factor of the dust, and $\epsilon_{dust} \leqslant 1$ is an efficiency expressing the fraction of the incident radiation that is re-emitted by the dust in the IR.

As shown in Reusch et al. (2022), the time evolution of the IR luminosity for AT2019fdr is well described by convolving the observed OUV luminosity with a (normalized) box function $B(t)$ centered at time Δt and having width $2\sigma_t$ (i.e., $B(t) = 1/(2\sigma_t)$ if $\Delta t - \sigma_t \leqslant t \leqslant \Delta t + \sigma_t$ and $B(t) = 0$ elsewhere, with $\sigma_t \leqslant \Delta t$). Such a function models the fact that a wide spread in time delays is expected due to the extended shape of the dust torus; see Figure 1. The quantity σ_t describes such a spread, with Δt being the central value. Following Reusch et al. (2022), we choose $\sigma_t = \Delta t$, which accounts for a portion of the IR flux to have zero delay due to some dust being along the line of sight. The time-differentiated version of Equation (13) reads

$$L_{IR}(t) = \epsilon_{bol}^{IR} \, \epsilon_{\Omega} \, \epsilon_{dust} \int_{-\infty}^{+\infty} L_{BB}^{bol}(t') \, B(t - t') \, dt'. \tag{14}$$

We performed a least-squares fit of the IR luminosity measurements at different times (taken from van Velzen et al. 2021a; Reusch et al. 2022), with the goal of obtaining: (i) a best-fit IR light curve; (ii) an estimate of the unabsorbed OUV luminosity and temperature, and (iii) information on the size and geometry of the dust torus. Results are given in Table 1; below, a more detailed description of the methodology is given.

The IR light curve was modeled as in Equation (14), with the assumption that the time profile of L_{BB}^{bol} is the same as that of the *observed* OUV luminosity, L_{BB}. The results of the fit are the time delay, Δt, and the normalization E_{IR}. For all three TDEs, the obtained best-fit IR light curve is in good agreement with the data. For AT2019fdr, it is consistent with the one shown in Reusch et al. (2022). For AT2019dsg, the light curve underestimates the earliest-measured IR flux, but fits the later data points very well.[11]

Setting the unknown coefficients in Equation (13) to optimistic (large) values, where we took $\epsilon_{\Omega} \, \epsilon_{dust} = 0.5$, and

estimating the correction factor ϵ_{bol}^{IR} for the W1 and W2 bands,[12] a minimum value E_{BB}^{bol} (min.), and therefore L_{BB}^{bol} (min.) $= E_{BB}^{bol}$ (min.) $\cdot L_{BB}/E_{BB}$ was obtained. From that estimate L_{BB}^{bol} (min.), the temperature of the OUV spectrum can be inferred from the Stefan-Boltzmann law; the result was adopted as the best estimate available for AT2019aalc (in the absence of an estimate from the observed spectrum), and served as a consistency check for the remaining two TDEs. See Table 1 for our results, the L_{BB}^{bol} (min.) and $L_{IR}^{bol} = (\epsilon_{bol}^{IR})^{-1} L_{IR}$ light curves are includes in our results figures (Figures 4, 7, and 10, upper rows) as black dotted and dashed–dotted curves, respectively.

3. Moderate-energy Protons Interacting with X-Rays (Model M-X)

Model-specific description. Our model M-X uses a low maximal proton energy $E_{p,max} = 5 \, 10^6$ GeV, universal for all TDEs, which is large enough to guarantee interactions with the X-ray targets in all TDEs, but low enough to suppress the interactions with the OUV; it therefore has the lowest requirement on the proton acceleration efficiency. The microphysics is illustrated in the cartoon in Figure 2, left panel, and model-specific assumptions and results are listed in the table in Figure 2, right panel. The radiation zone is determined by the location of the accelerator, $R \simeq R_{acc} \gtrsim R_{BB}$. For the sake of simplicity, we choose $R = 5 \, 10^{15}$ cm together with $B = 1$ G for all three TDEs to satisfy the magnetic confinement condition in Equation (8) for the maximal proton energies used here. This means that injected protons will gyrate in magnetic fields and interact with X-rays and protons of the outflow to produce neutrinos, as illustrated in the cartoon.

All three TDEs have in common that they have been observed in X-rays, which are the prime target for the neutrino production of 100 TeV neutrinos; see Equation (1). However, the X-ray observations have very different characteristics: an exponential early decay (AT2019dsg; Stein et al. 2021b; van Velzen et al. 2021b), a late-time observation with strongly varying limits at different times (AT2019fdr; Reusch et al. 2022), and a late-term constant flux ("plateau") significantly after the neutrino observation (AT2019aalc; van Velzen et al. 2021a). Since X-rays are expected to originate from the accretion disk, the TDE unified model predicts obscuration effects depending on the viewing angle (Dai et al. 2018), and as large temperature fluctuations on short timescales may be unlikely, we hypothesize that the (highest) detected X-ray signal is indicative for the actually emitted X-ray flux, and that obscuration beyond R, such as from a complicated geometry or outflow, leads to the observed fluctuations.[13] For example, following the slim disk model (Wen et al. 2020), the unobscured flux will be relatively stable over time, except when it changes or ceases when the mass accretion rate drops below the Eddington luminosity—such as if there is a transition of the accretion disk state. Therefore we suppress it exponentially with a factor $\propto \exp(-L_{edd}/\dot{M})$, which implies that the X-ray flux available for interactions is stable over t_{dyn}. Consequently, we use the measured X-ray temperature T_X for each TDE, and we normalize the spectrum at the time of the

---

[11] The discrepancy at early times might be an indication that the simple model in Equation (14) is inaccurate. A possible improvement on it could be to use a bimodal distribution instead of a box function, to account for the presence of dust on *both* sides of the line of sight, with one side being closer to the observer (resulting in a smaller time delay) than the other.

[12] Here we use thermal spectra with either the measured IR temperature (for AT2019fdr) or a theoretically motivated value close to the dust sublimation temperature (for AT2019dsg and AT2019aalc); we find $(\epsilon_{bol}^{IR})^{-1} \simeq 1.26$, 1.38 in the two cases (factors correcting the combined W1 +W2 luminosity νL_ν).

[13] For AT2019dsg, the same effect has led to X-ray isotropization of external target photons in the jetted model (Winter & Lunardini 2021), where the assumed $R_{acc} \simeq R_{BB}$ was somewhat smaller.
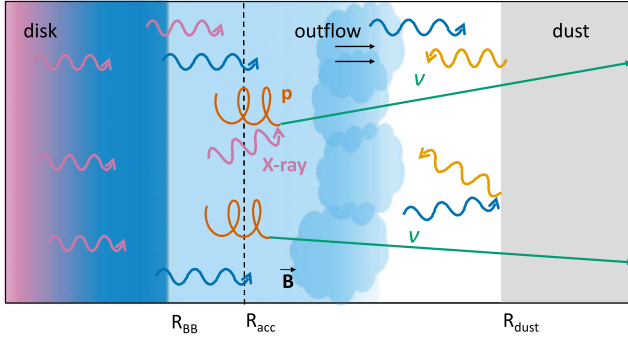
	AT2019dsg	AT2019fdr	AT2019aalc
Model assumptions			
R [cm]	$5.0\,10^{15}$	$5.0\,10^{15}$	$5.0\,10^{15}$
$E_{p,\max}$ [GeV]	$5.0\,10^{6}$	$5.0\,10^{6}$	$5.0\,10^{6}$
B [G]	1.0	1.0	1.0
Model results			
N_ν GFU	0.048	0.0048	0.070
	(0.012)	(0.0012)	(0.018)
N_ν PS	0.50	0.077	3.3
	(0.12)	(0.019)	(1.8)

Figure 2. Model M-X. Left panel: microphysics cartoon. Right panel: model assumptions and results. See caption of Figure 4 for the definition of the GFU (gamma-ray follow-up) and PS (point-source) effective areas. Predicted event rates are for $\varepsilon_{\mathrm{diss}} = 0.2$ (0.05).

highest measured energy flux to the X-ray measurement in the respective energy range—however we quote bolometric X-ray luminosities in Table 1. The in-source photon density n_X can be computed from L_X using Equation (10). Note that since L_X hardly changes over time, the neutrino time delay cannot be generated by the X-ray target in our model; including fluctuations of L_X would result in corresponding time variations of the neutrino light curve.

Interaction rates and calorimetric behavior. It is useful to look at the rates (inverse timescales) as a function of energy for one example to illustrate the calorimetric behavior; therefore, we show in Figure 3 the rates for AT2019dsg at peak time (solid curves) and at the time of the neutrino emission (dashed curves, where time-dependent). First of all, we note that $p\gamma$ interactions with X-rays are possible for $E < E_{p,\max}$, whereas the interactions with the OUV BB are suppressed because the proton energies are too low (the gray-shaded area marks $E > E_{p,\max}$). However, since the OUV luminosity is much higher than the X-ray luminosity, and Bethe–Heitler pair production has a lower threshold, the rate of pair production off OUV photons $t_{p,\mathrm{BH}}^{-1}$ (see Section 4 for the implementation) can be substantial.[14] Depending on the ratio between OUV and X-ray luminosities, X-ray $p\gamma$ interactions may be subdominant. Since the OUV luminosity scales with the mass accretion rate, the corresponding Bethe–Heitler rate will be lower at the neutrino emission time t_ν—whereas the X-ray part of $t_{p\gamma}^{-1}$ is quite stable (dashed curves). We observe that while this effect suppresses the overall neutrino production and leads to low neutrino event rates (see Figure 2, right panel), it favors a late-term neutrino production.[15] Proton-proton interactions are always relevant for the neutrino production below the $p\gamma$ threshold, but inefficient in the shown example compared to the X-ray interactions; a counter-example is AT2019aalc for which the observed X-ray flux is low.

We can also discuss the proton confinement and calorimetric behavior using Figure 3. Here the free-streaming escape rate t_{fs}^{-1} is much larger than t_{dyn}^{-1}, and X-ray interactions are effective over the dynamical timescale, but not over the free-streaming timescale. Since protons at the highest energies are confined ($t_{p,\mathrm{esc}}^{-1} \lesssim t_{\mathrm{dyn}}^{-1} \ll t_{p\gamma}^{-1}$), they accumulate, and the in-source proton density will increase. As a result, the $p\gamma$ interactions will be
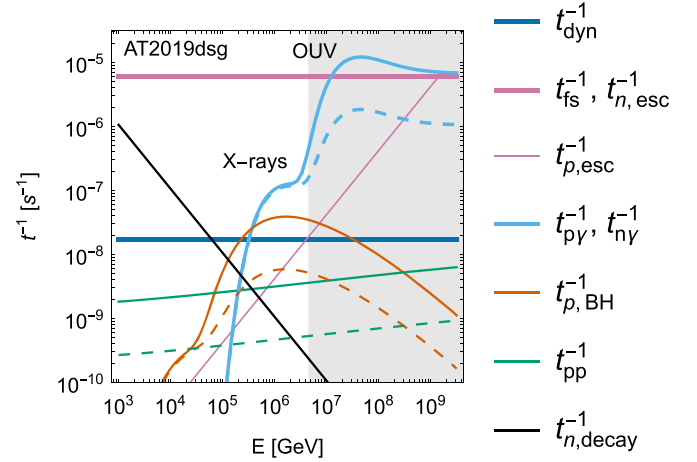

Figure 3. Relevant inverse timescales (rates) for protons and neutrons for M-X and AT2019dsg in the SMBH frame as a function of energy (in the observer's frame); the shaded area is beyond $E_{p,\max}$ for M-X. Solid curves refer to the t_{peak}, whereas dashed curves refer to the time of the neutrino emission t_ν (unless the rate is constant in time). Note that for $p\gamma$ and pp interactions, the interaction rates (and not the cooling rates) are shown.

stretched over a longer timescale—leading to a delay of the neutrino production, scaling with $t_{p\gamma}$. This can be also seen in analytical estimates: the optical thicknesses for the free-streaming and calorimetric cases can, for the X-rays, be analytically roughly estimated as[16]

$$\tau_{p\gamma}^{\mathrm{fs}} \equiv \frac{t_{\mathrm{fs}}}{t_{p\gamma}} \simeq 0.06 \left(\frac{L_X}{10^{44}\,\mathrm{erg\,s^{-1}}}\right)\left(\frac{T_X}{100\,\mathrm{eV}}\right)^{-1}\left(\frac{R}{5\,10^{15}\,\mathrm{cm}}\right)^{-1}$$

$$\tau_{p\gamma}^{\mathrm{cal}} \equiv \frac{t_{\mathrm{dyn}}}{t_{p\gamma}} \simeq 18 \left(\frac{L_X}{10^{44}\,\mathrm{erg\,s^{-1}}}\right)\left(\frac{T_X}{100\,\mathrm{eV}}\right)^{-1}\left(\frac{R}{5\,10^{15}\,\mathrm{cm}}\right)^{-2}$$

$$\times \left(\frac{t_{\mathrm{dyn}}}{600\,\mathrm{days}}\right), \qquad (15)$$

---

[14] The effect has also been pointed out in Murase et al. (2020b) for the hidden wind model, specifically.

[15] For AT2019dsg, the X-ray interaction rate always dominates over $t_{p,\mathrm{BH}}^{-1}$; for AT2019fdr, X-ray interactions at t_{peak} are suppressed, but are more efficient at t_ν; for AT2019aalc, X-ray interactions are always suppressed.

[16] For these analytical estimates, we follow the method in Guetta et al. (2004) using $t_{p\gamma}^{-1} \simeq \sigma_{p\gamma}\,n_X\,c$, where n_X is the target number density and $\sigma_{p\gamma} \simeq 500\,\mu\mathrm{barn}$. The photon number density is estimated from the photon energy density divided by the peak energy of $2.8\,T_X$ (Fiorillo et al. 2021; where the number density peaks); the estimate therefore only applies to the spectral peak. Compared to numerical computations, for which we follow Hummer et al. (2010), and which take into account the full energy dependence of the cross section and the pitch-angle averaging, the optical thickness is typically slightly overestimated (by a factor of a few) in the analytical case because of spectral effects and the neglected width of the Δ-resonance/pitch-angle averaging (Hummer et al. 2012).

which means that $\tau_{p\gamma}^{\rm fs} < 1$, but $\tau_{p\gamma}^{\rm cal} > 1$—so the system is optically thin, but calorimetric. A small subtlety are neutrons produced in $p\gamma$ interactions, for which free-streaming escape dominates over interactions and decays ($t_{n,\rm decay}^{-1} = m_n/(E\tau_0)$ with an assumed rest-frame lifetime $\tau_0 \simeq 885$ s; see black line in Figure 3); the effective proton cooling rate is therefore closer to the (shown) interaction rate than $0.2 \, t_{p\gamma}^{-1}$. Our numerical code treats all of these effects self-consistently, as pointed out earlier.

Results. Our main results for model M-X are presented in Figure 4 for all three TDEs (columns). The upper row shows the time evolution of the luminosities (in the SMBH frame), and the lower row reports the muon neutrino fluences and expected event rates, as well as the contributions from different targets. Flavor mixings are taken into account using the mixing angles in Esteban et al. (2020). Concerning the time evolution (upper row), the proton injection luminosity follows the OUV BB luminosity (black dotted curves) in all cases. It scales proportionally to the Eddington luminosity (green dashed curves), so that at $t_{\rm peak}$ (by our assumptions) $L_p = \varepsilon_{\rm diss} F_{\rm peak} L_{\rm edd} \simeq (5-20) L_{\rm edd}$ goes into nonthermal proton injection. The accumulated in-source proton density N_p in Equation (3) drives the neutrino production rate $J_\nu \propto N_p \, t_{p\gamma}^{-1}$ (with $t_{p\gamma}^{-1} \propto L_X$) in the radiation zone (see Hummer et al. 2010 for details); N_p however cannot be directly shown in the figure because it is a density differential in energy and not in time; we consequently show a related effective luminosity integrated over the highest energies (chosen to be above the $p\gamma$ threshold, and therefore most relevant to neutrino production):

$$L_{p,\rm cal}^{\rm eff}(t) \equiv t_{\rm fs}^{-1} \int_{E_{p,\rm max}/3}^{E_{p,\rm max}} E_p \, N_p(E_p, t) \, dE_p, \qquad (16)$$

see green dashed–dotted curves (in arbitrary units). We see that $L_{p,\rm cal}^{\rm eff}$ first increases with the proton injection, then it decays with a delay determined by $p\gamma$ interactions. The (unattenuated) X-ray luminosities are shown as blue curves, normalized to the highest observed luminosity (blue dots). The neutrino light curves, at the leading order, then follow the product $L_{p,\rm cal}^{\rm eff} \times L_X$, but OUV and pp interactions also contribute somewhat. Since L_X is assumed to be roughly constant over $t_{\rm dyn}$, $L_{p,\rm cal}^{\rm eff}$ dominates the behavior of the neutrino light curve. The calorimetric behavior leads to a deviation between the solid (L_p) and dashed–dotted ($L_{p,\rm cal}^{\rm eff}$) green curves here: if free-streaming escape dominated in Equation (3), the dashed–dotted curve would follow the solid curve ($L_{p,\rm cal}^{\rm eff} \propto N_p \simeq J_p \, t_{\rm fs} \propto L_p$)—whereas magnetically confined protons accumulate ($L_{p,\rm cal}^{\rm eff} \propto N_p \simeq \int J_p \, dt \propto \int L_p \, dt$) and lead to $L_{p,\rm cal}^{\rm eff}$ being extended in time over a period comparable to $t_{\rm dyn}$. The observed neutrino times are marked by arrows; the best description of the neutrino delay (peak consistent with arrow) is obtained for AT2019aalc and the worst for AT2019dsg (because of the quickly decaying BB). It is noteworthy that in all cases, the neutrino luminosities (at the sources) are comparable, and the fluences at Earth are strongly affected by the redshifts.

The lower row of Figure 4 shows the neutrino fluences, which, for AT2019dsg and AT2019fdr, are dominated by X-ray interactions (blue dashed–dotted curves) with smaller contributions from the other targets. For AT2019aalc, the observed X-ray luminosity was very low (see upper-right panel), which means that indeed pp interactions dominate here. The neutrino fluence is suppressed beyond about 20 TeV by Bethe–Heitler pair production off the OUV target photons. In the figure (as well as Figure 2, right table) the neutrino event rates for the gamma-ray follow-up (GFU) and point-source (PS) effective areas are shown for the respective decl. band (that is similar for all TDEs).[17] A comparison of the GFU event number prediction with the expectation in Table 1 (for GFU, obtained in the listed references from counting statistics) indicates that (for both values of $\varepsilon_{\rm diss}$) the prediction for AT2019dsg is in the expected range, that for AT2019fdr it is slightly below, and that for AT2019aalc (for which no comparison exists) it is high. In fact, the source may appear in point-source analyses. This indicates that $\varepsilon_{\rm diss} \gtrsim 0.1$–0.2 here, and it might be slightly different for the three TDEs.

The predicted neutrino energies from X-ray interactions match observations very well (arrows), as expected; we note, however, that the probable neutrino energy has a range, illustrated by the gray areas in the figure (see figure caption for description), which extends to higher energies—derived for an E^{-2} input spectrum, though.

Discussion. Particle acceleration may occur in high-velocity winds embedded in the TDE debris (Murase et al. 2020b) or shocks from stream crossings (Hayasaki & Yamazaki 2019). Compared to Murase et al. (2020b), our production region is typically slightly smaller (than 10^{16} cm) and our required cosmic-ray injection luminosity (which was normalized to the BB luminosity in that paper) is higher, as can be seen in Figure 4 (upper row). This means that in the hidden wind models, it may be difficult to achieve high enough proton luminosities (i.e., $\varepsilon_{\rm diss}$) at least from the estimates in Murase et al. (2020b). Magnetic confinement is also considered in the hidden wind model, where, however, adiabatic losses limit the optical thickness. In the hidden wind models, pp interactions with the debris can also play a major role; however, large uncertainties are implied, such as from the geometry and the time evolution of the system. There are also some similarities with the TDE outflow model for AT2019dsg in Wu et al. (2022): outflow–cloud interactions may lead to particle acceleration, and pp interactions with the clouds may lead to neutrino production. While the production region in that model is a bit larger ($R \simeq 10^{16}$ cm), the pp interactions are efficient in the clouds, which are assumed to have a size of about $\simeq 10^{14}$ cm and act as calorimeters. Our pp interactions with the outflow itself are less efficient because our production radius is large (the target density is about a factor 50 smaller), and therefore the effect is subdominant for AT2019dsg see Equation (11). We note however that the shocks generated by the outflow–cloud interactions may be an interesting acceleration site. For a comparison/discussion of jetted models, see Appendix A. Furthermore, if the radiation zone is expanding—such as expected in the wind models—adiabatic cooling can affect especially model M-X; see Appendix B. We do not consider this effect in the main text because it does not apply to accelerators with a stable radiation zone, and we anticipate that winds or outflows as

---

[17] The predicted event rates are computed by folding the predicted fluences with the corresponding effective areas over the full energy ranges: $N_\mu = \int \mathcal{F}_{\nu_\mu}(E_\nu) \, A_{\rm eff}(E_\nu) \, dE_\nu$. The GFU effective area includes the trigger probability of the gamma-ray follow-up pipeline, which implies that it has a higher energy threshold than the PS effective area. The GFU event rates should be used for a comparison to the actual observations from neutrino follow-ups, whereas the PS event rates are predictions relevant to evaluate if the source would appear in independent point-source analyses; see discussion below and in Section 7.
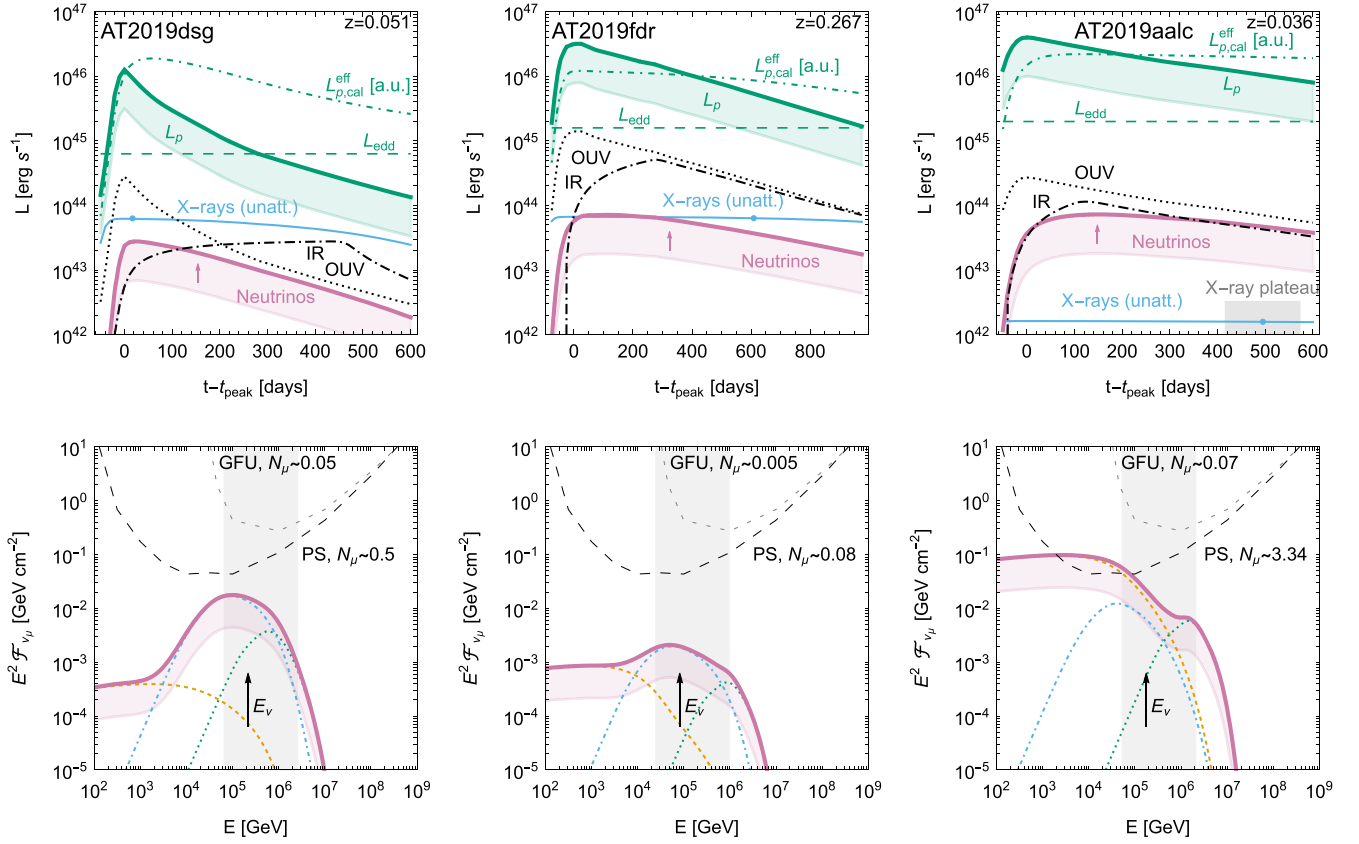
Figure 4. Time-dependent evolution of the luminosities (upper row) and neutrino fluences (lower row) for model M-X. In the upper row, our OUV (black dotted) and IR (black dashed–dotted) curves are shown as bolometric luminosities, OUV before dust attenuation. The X-ray curves show the assumed bolometric unattenuated evolution from the disk, and measurements are marked by dots. We also show the assumed proton injection luminosity L_p and the in-source proton density as effective luminosity $L_{p,cal}^{eff}$ integrated over the highest proton energies (arbitrary units; see the main text for definition). The neutrino observation times are marked by arrows. In the lower row, the total neutrino fluence is shown, as well as its origin from different targets (outflow pp: dashed orange, X-rays: blue dashed–dotted, OUV: green dotted). In addition, the GFU (Blaufuss et al. 2019) and PS (Aartsen et al. 2014) differential limits $E_\nu^2 \mathcal{F}_{\nu_\mu} = E_\nu / (A_{eff}(E_\nu) \ln 10)$ are shown together with the integrated muon neutrino event rates (all events are in the same decl. band). The most likely neutrino energies are marked, and gray-shaded areas mark the 99.73% CL expected neutrino energy ranges expected for an E^{-2} neutrino flux following the method in Palladino & Winter (2018). Colored shadings correspond to varying ε_{diss} in the interval $\varepsilon_{diss} = 0.05$–2 (from lower to upper curves); ε_{diss} enters as a multiplicative parameter in the proton injection and neutrino luminosities; see Equation (5).

accelerators are furthermore challenged by the high required ε_{diss}. Off-axis jets may be an alternative especially since the calorimeter leads to the isotropization of protons emitted into different directions; here the emission radius of the cosmic rays would need to match R—which is quantitatively comparable to the collision radius expected for internal shocks (Lunardini & Winter 2017). The potential contributions from core models cannot be captured by our approach because of the assumption $R \gtrsim R_{BB}$, which means that accelerators in the core (where interactions are more efficient) cannot be well described for model M-X.

Finally we note that in all cases an average neutrino delay $t_\nu - t_{peak}$ in the right ball park is expected, originating in the calorimetric behavior of the system. However, the neutrino light curves are widely spread in time, and a slight preference of an early neutrino emission closer to the peak is implied in the cases with higher $p\gamma$ efficiencies—which have the effect of depleting the available in-source protons. Thus, a high neutrino production efficiency and a long neutrino delay are anticorrelated for model M-X. An exception is AT2019aalc where (slow) pp interactions dominate and the neutrino flux peaks at lower energies. Ways to improve the neutrino time dependence emerge if the nonthermal proton injection is delayed with respect to the mass fallback rate. Note that in all cases the actual X-ray emission may be even higher than the observation, since the observed flux may be obscured as

well. However, this may be unlikely for AT2019aalc where the observed X-ray flux was stable over the duration of a few hundred days (called "X-ray plateau" in figures).

4. Medium-energy Protons Interacting with Optical-UV Photons (Model M-OUV)

Model-specific description. In order to foster interactions with the OUV target photons, $E_{p,max} = 1 \cdot 10^8$ GeV, higher than for M-X, is used here. The microphysics is illustrated in the cartoon in Figure 5, left panel, and model assumptions and results are listed in the table in Figure 5, right panel. If $R_{acc} \lesssim R_{BB}$, the radiation zone is determined by the BB radius $R \simeq R_{BB}$ for M-OUV, for which we use measured or estimated values listed in the table. While possible accelerators could (in principle) be disk or corona, we assume for the sake of simplicity of computation that $R_{acc} \sim R \sim R_{BB}$.[18]

---

[18] This implies that, for the sake of generality, we neglect additional interactions with X-rays in the core (small R_{acc}). For X-rays, the optical thickness increases with decreasing injection radius R_{acc} as long as $R_{acc} > R_X$ (beyond the X-ray photosphere). However, it can be estimated that in the core, $\tau_{p\gamma}^{fs}$, describing the X-ray interactions in Equation (15), is for $R \gtrsim R_S$ (for $M = 10^7 M_\odot$) smaller than $\tau_{p\gamma}^{fs}$ in Equation (17), describing the OUV interactions for $R \simeq R_{BB}$. This means that the additional core contributions are smaller than the ones off the OUV target for the chosen parameters and comparable proton injection luminosities.
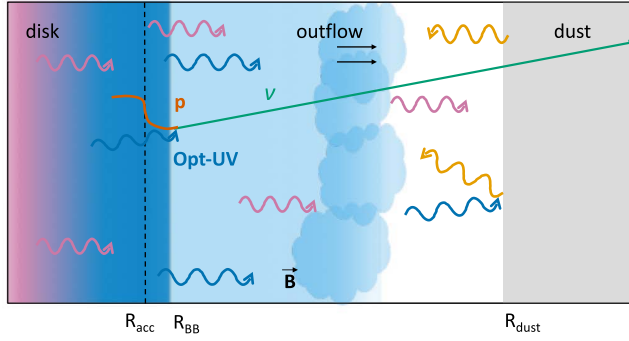
	AT2019dsg	**AT2019fdr**	**AT2019aalc**
Model assumptions			
R [cm]	$5.0\,10^{14}$	$4.9\,10^{15}$	$1.0\,10^{16}$
$E_{p,\mathrm{max}}$ [GeV]	$1.0\,10^8$	$1.0\,10^8$	$1.0\,10^8$
B [G]	0.1	0.1	0.1
Model results			
N_ν GFU	0.21	0.055	1.2
	(0.052)	(0.014)	(0.29)
N_ν PS	1.1	0.22	3.6
	(0.28)	(0.054)	(0.90)

Figure 5. Model M-OUV. Left panel: microphysics cartoon. Right panel: model assumptions and results. Here $R \sim R_{\mathrm{BB}}$ from van Velzen et al. (2021b; AT2019dsg) and from Reusch et al. (2022; AT2019fdr), whereas it is an assumption for AT2019aalc. Predicted event rates are for $\varepsilon_{\mathrm{diss}} = 0.2$ (0.05).

While the OUV luminosity has been measured for all three TDEs, a dust echo has been measured as well in each case. Its intensity implies that the actual BB luminosity at R_{BB} must be significantly higher than the observed luminosity; we therefore derived in Section 2.5 an estimate for the minimal bolometric luminosity; see Table 1. Furthermore, the target photon density in the BB photosphere is estimated by the free-streaming assumption Equation (10), which is conservative if $R_{\mathrm{acc}} < R_{\mathrm{BB}} \simeq R$, and more accurate if $R_{\mathrm{acc}} \simeq R \gtrsim R_{\mathrm{BB}}$. Therefore, we anticipate that our neutrino prediction for M-OUV is on the conservative side, and the actual neutrino fluence could be somewhat higher.

Interaction rates and optically thick behavior. In Figure 6, we show the rates (inverse timescales) as a function of energy for AT2019dsg as an example, for the parameters chosen for M-OUV; again solid curves refer to peak time and dashed curves to the time of the neutrino emission. Here $E_{p,\mathrm{max}}$ is high enough that interactions with the OUV target are possible— and, in fact, they dominate even at the time of the neutrino emission. The optical thickness to $p\gamma$ interaction can be analytically estimated as

$$\tau^{\mathrm{fs}}_{p\gamma} \equiv \frac{t_{\mathrm{fs}}}{t_{p\gamma}} \simeq 300 \left(\frac{L_{\mathrm{BB}}}{10^{45}\ \mathrm{erg\ s^{-1}}} \right) \left(\frac{T_{\mathrm{BB}}}{\mathrm{eV}} \right)^{-1} \left(\frac{R}{10^{15}\ \mathrm{cm}} \right)^{-1}, \quad (17)$$

which means that typically $\tau^{\mathrm{fs}}_{p\gamma} \gg 1$ at peak, and the system is optically thick, and protons and neutrons cool efficiently by $p\gamma$ interactions.

X-ray and pp interactions may still contribute at lower energies over the dynamical timescale, as the $p\gamma$ interaction rate off X-rays is higher than the (diffusive) escape rate. While the OUV interaction time is of the order of hours, the neutrinos from X-ray and pp interactions tend to come later. Nevertheless, it is clear already from the interaction rates that the dominant contribution to the neutrino signal (from OUV interactions) will follow the BB evolution on the hour scale.

Results. Figure 7 displays our main results in the same format as Figure 4. Here the neutrino light curves (reddish-purple curves in upper panels) follow the product of $L^{\mathrm{eff}}_{p,\mathrm{cal}}$ (green dashed–dotted curve) and $L^{\mathrm{bol}}_{\mathrm{BB}}$ (min.; black dotted curve) at the leading order. As expected, it is more difficult to reproduce the neutrino time delay marked by the reddish-purple arrows. Here $L^{\mathrm{eff}}_{p,\mathrm{cal}} \propto N_p \simeq J_p\, t_{p\gamma} \propto L_p\, L^{-1}_{\mathrm{BB}}$ from Equation (3). The fact that both L_p and L_{BB} have the same time dependence by construction (L_p follows the BB light curve, and the interaction rate depends on that as well) explains why $L^{\mathrm{eff}}_{p,\mathrm{cal}}$ declines over time more slowly than L_p, until at later times,
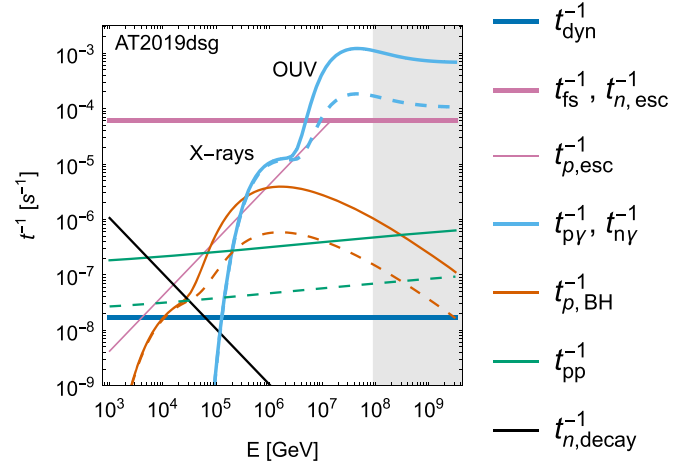

Figure 6. Relevant inverse timescales (rates) for protons and neutrons for M-OUV and AT2019dsg in the SMBH frame as a function of observed energy. For details, see the caption of Figure 3.

escape takes over as the leading radiation mechanism. It is not a calorimetric behavior here, but a consequence of the explicit time dependence of the injection and target luminosities. The neutrino luminosity is $\propto L^{\mathrm{eff}}_{p,\mathrm{cal}} \times L_{\mathrm{BB}}$, and therefore it, to first approximation, follows the strong time dependence of L_{BB}.

The neutrino fluences in the lower row (see also Figure 5, right table) are higher than for model M-X, and are all within the expected ranges in Table 1. The peaks are all dominated by the BB interactions (green dotted curves) thanks to the requisitely high proton energies, whereas X-rays (blue dashed–dotted curves) and pp (orange dashed curves) interactions contribute at lower energies. The predicted neutrino energies are significantly higher than the most likely energies (black arrows), but are plausible if the uncertainties (gray areas) are taken into account. It is noteworthy that AT2019aalc exhibits event rates $N_\mu > 1$ for both the GFU and PS effective areas—if $\varepsilon_{\mathrm{diss}}$ is largest, $\varepsilon_{\mathrm{diss}} = 0.2$, in spite of the relatively large assumed value for R. This means that, while the observation of AT2019dsg and AT2019fdr may have been a coincidence motivated by the Eddington bias, AT2019aalc is a neutrino source that could have been detected independently as neutrino point source.

Discussion. While M-OUV exhibits higher event rates than M-X, it offers a poorer description of the neutrino time delay, and the size of the system plays only a minor role in this. A possible solution of this problem might be that the neutrino delay comes from a delayed proton injection itself, for which
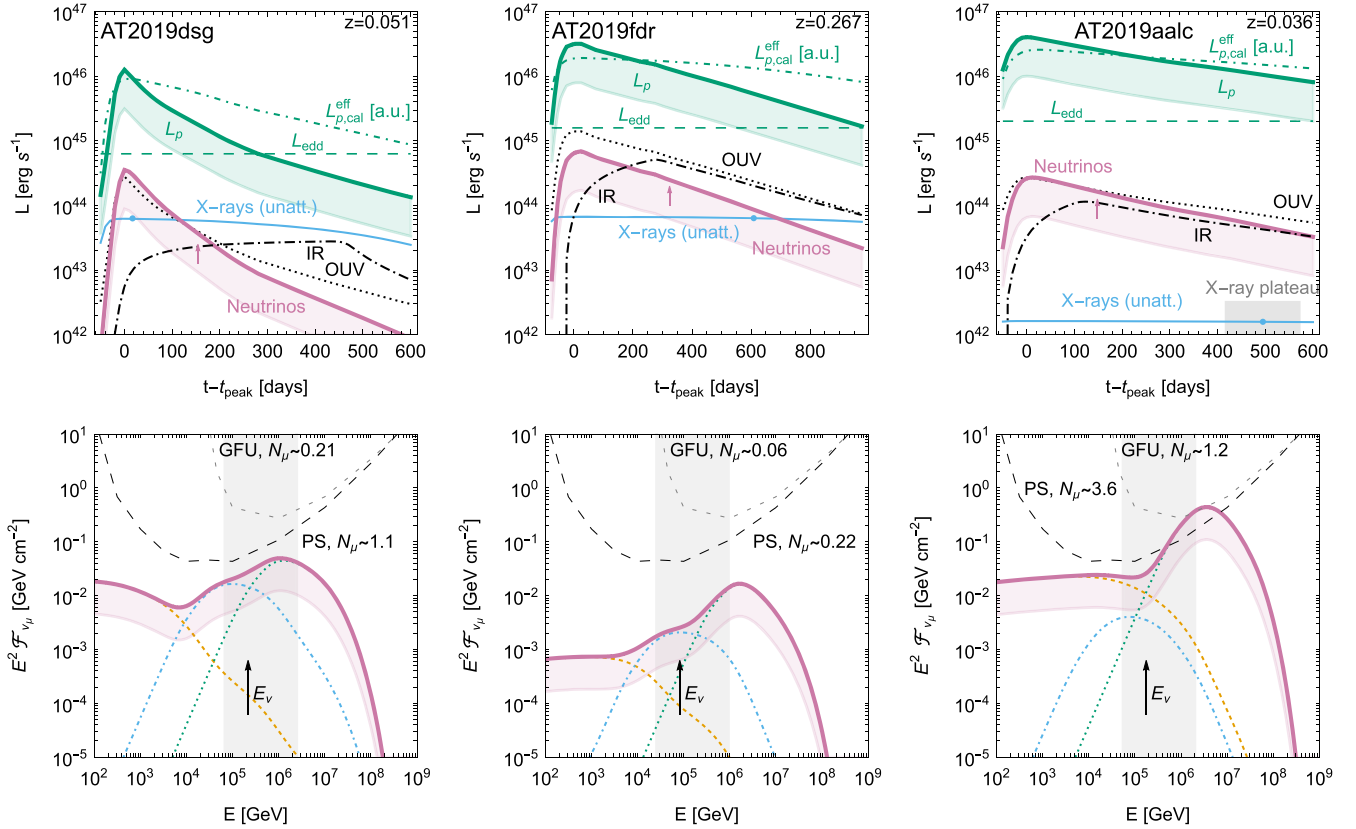
Figure 7. Time-dependent evolution of the luminosities (upper row) and neutrino fluences (lower row) for model M-OUV. For details, see the caption of Figure 4.

we could however not yet identify a physical motivation. The strength of model M-OUV is that high neutrino fluences can be produced, given that the estimates for the unobscured BB luminosities are lower limits only. Comparing the expected number of neutrinos in Table 1 with the predicted ones in Figure 5 (right table), one finds that $\varepsilon_{\rm diss} \gtrsim 0.03$ satisfies all requirements.

As pointed out earlier, our model M-OUV is a quantitative implementation of the original analytical estimate in Stein et al. (2021b) for AT2019dsg; therefore, we have performed numerical cross-checks for similar parameters to isolate the differences. From Figure 7, upper left panel, we can see that the neutrino luminosity is about $L_p/40$ at $t_{\rm peak}$, whereas the original model predicts a factor $L_p/8$ in the optically thick case. The main difference comes from the bolometric correction: our L_p is related to the full nonthermal proton spectrum, not only to the part beyond the pion production threshold. A smaller contribution comes from the pitch-angle averaging and width of the cross section taken into account in numerical computations. Furthermore, note that the optical thickness drops as a function of time, which overall leads to a significantly lower neutrino event rate prediction than the analytical estimate taken at the BB peak.

Let us discuss possible accelerator realizations. First of all, note that if an explicit acceleration rate is considered, the $E_{p,\rm max}$ in Figure 6 cannot be self-consistently reached if the radiation and acceleration zones are identical; see discussion in Appendix C. Therefore, a different, possibly more compact acceleration region below the OUV photosphere with stronger magnetic fields is implied, which might be a disk or corona; however, note that requisitely high proton energies must be reached, which seems challenging for stochastic acceleration (Murase et al. 2020a). An

off-axis jet is unlikely here, because the cosmic rays would interact faster than they can isotropize, which means that the neutrinos would propagate in the jet direction (see Appendix A), whereas wind or outflow models are disfavored for M-OUV because they typically require $R \gg R_{\rm BB}$.

5. Ultra-high-energy Protons Interacting with Infrared Photons (Model M-IR)

Model-specific description. The fact that all three neutrino-observed TDEs have been associated with strong dust echoes suggests a direct connection of the neutrino production with the IR photons from the dust echoes. Even more: the dust echo light curves, shown as dashed–dotted black curves in our results plots (e.g., Figure 4), seem to directly suggest being the origin of the neutrino time delay (see arrows for neutrino arrivals), because the neutrinos arrive at or close to the peak of the dust echo.[19]

The microphysics of model M-IR is illustrated in the cartoon in Figure 8, left panel, and model assumptions and results are listed in the table in Figure 8, right panel. The challenges here are the ultra-high required proton and corresponding neutrino energies; we use a TDE-universal $E_{p,\rm max} = 5 \, 10^9$ GeV; see Equation (1) and discussion thereafter. The scattering and reprocessing of the OUV (perhaps even X-ray) photons in the dust leads to a delayed IR signal to the observer, as outlined in Section 2.5; isotropized IR photons will correspondingly fill the production volume with $R \simeq R_{\rm dust}$. The inferred $R_{\rm dust}$ of the order of 10^{17} cm is typically a rough estimate from the time

---

[19] For AT2019dsg, the dust echo peaks much later, but the OUV light curve peaks much earlier, which may compensate for the delay.
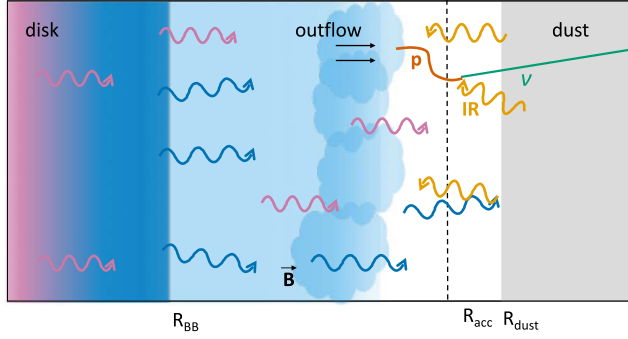
	AT2019dsg	AT2019fdr	AT2019aalc
Model assumptions			
R [cm]	$5.0\,10^{16}$	$2.5\,10^{17}$	$2.0\,10^{17}$
$E_{p,\max}$ [GeV]	$5.0\,10^{9}$	$5.0\,10^{9}$	$5.0\,10^{9}$
B [G]	0.1	0.1	0.1
Model results			
N_ν GFU	0.030	0.013	0.036
	(0.0074)	(0.0032)	(0.091)
N_ν PS	0.074	0.024	0.62
	(0.019)	(0.0060)	(0.16)

Figure 8. Model M-IR. Left panel: microphysics cartoon. Right panel: model assumptions and results. Here R is taken from Stein et al. (2021b; radio), Reusch et al. (2022; IR) and Table 1 ($c\,\Delta t$) for AT2019dsg, AT2019fdr, and AT2019aalc, respectively. Predicted event rates are for $\varepsilon_{\rm diss} = 0.2$ (0.05).
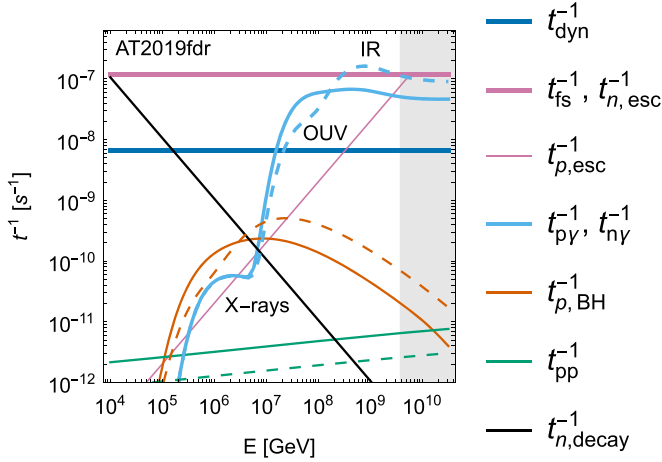

Figure 9. Relevant inverse timescales (rates) for protons and neutrons for M-IR and AT2019fdr in the SMBH frame as a function of observed energy. For details, see the caption of Figure 3.

role here, and so does Bethe–Heitler pair production. However, the interactions with the OUV photons, which have a higher luminosity but not necessarily number density, cannot be neglected. At $t_{\rm peak}$, the system is optically thin to $p\gamma$ interactions; however, confined protons will interact over $t_{\rm dyn}$ with the OUV and IR targets similarly to M-X. At t_ν, the interactions with IR photons from the dust echo in fact dominate the neutrino production.

The analytical estimates for the optical thicknesses in the free-streaming and calorimetric cases and the IR target are

$$\tau_{p\gamma}^{\rm fs} \equiv \frac{t_{\rm fs}}{t_{p\gamma}} \simeq 3\left(\frac{L_{\rm IR}}{10^{44}\ {\rm erg\ s^{-1}}}\right)\left(\frac{T_{\rm IR}}{0.1\ {\rm eV}}\right)^{-1}\left(\frac{R}{10^{17}\ {\rm cm}}\right)^{-1},$$

$$\tau_{p\gamma}^{\rm cal} \equiv \frac{t_{\rm dyn}}{t_{p\gamma}} \simeq 60\left(\frac{L_{\rm IR}}{10^{44}\ {\rm erg\ s^{-1}}}\right)\left(\frac{T_{\rm IR}}{0.1\ {\rm eV}}\right)^{-1}\left(\frac{R}{10^{17}\ {\rm cm}}\right)^{-2}$$
$$\times \left(\frac{t_{\rm dyn}}{900\ {\rm days}}\right),$$

(18)

respectively. This means that the neutrino production from protons interacting with the IR target is guaranteed to be efficient over the dynamical timescale, and that the system may be optically thick. Assuming $t_{p\gamma,\rm cool} \simeq 5 \times t_{p\gamma}$ (such as in the optically thick case), it is also interesting that the proton interactions are slow:

$$t_{p\gamma,\rm cool} \simeq 70\ {\rm days}\left(\frac{T_{\rm IR}}{0.1\ {\rm eV}}\right)\left(\frac{L_{\rm IR}}{10^{44}\ {\rm erg\ s^{-1}}}\right)^{-1}\left(\frac{R}{10^{17}\ {\rm cm}}\right)^{2},$$

(19)

which helps the neutrino time delay, as the injected in-source protons will be depleted over that timescale.

Results. We present our main results for model M-IR in Figure 10. The neutrino light curves (reddish-purple curves in upper panels) follow the product of $L_{p,\rm cal}^{\rm eff}$ (green dashed–dotted curves) and OUV (black dotted curves) or IR (black dashed–dotted curves). Therefore, a different time evolution for the neutrinos from OUV and IR is expected. Here we re-discover a calorimetric behavior similar to M-X for AT2019fdr and AT2019aalc in which cases the neutrino time delay (reddish-purple arrows) can be easily reproduced from the time delay of the dust echo. On the other hand, AT2019dsg is free-
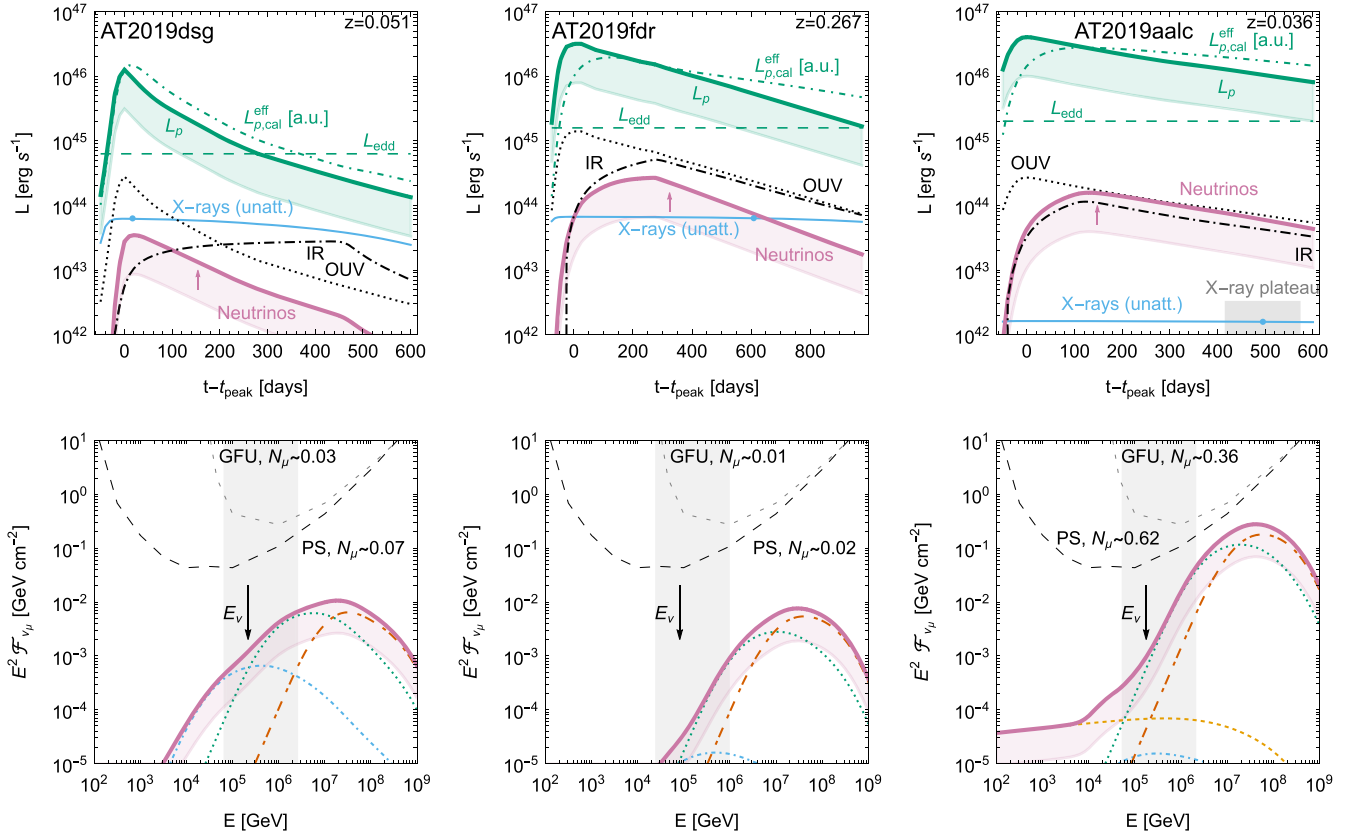
delay of the dust echo, subject to geometric uncertainties. We choose the values in Figure 8, right table, which are related to IR observations (AT2019fdr) or our dust model (AT2019aalc). For AT2019dsg, we note that too large values of R lead to too inefficient neutrino production; for our dust model, the observed Δt in Table 1 translates into $R_{\rm dust} \simeq 6\,10^{17}$ cm, i.e., the largest dust region—compared to the smallest $R_{\rm BB}$. Instead of this value, we use the size R inferred from the observed radio signal, speculating that the dust region may be more structured to satisfy all constraints. The chosen value for $B = 0.1$ G for all three TDEs leads to confinement of protons over such a large region (see Equation (8)), which helps the reproduction of the neutrino time delay. The IR luminosities and light curves are taken from our own dust model in Section 2.5, and the in-source density is computed with Equation (10).

Interaction rates and optically thick/calorimetric behavior. In Figure 9, we show the rates (inverse timescales) as a function of energy, this time for AT2019fdr as an example, for the parameters chosen for M-IR; again solid curves refer to peak time and dashed curves refer to the time of the neutrino emission. Here $E_{p,\max}$ is high enough that interactions with all targets are possible. We see that the free-streaming and dynamical timescales are much closer to each other than in the other models because of the larger size of the region; interactions with X-rays and with the outflow (pp) play a minor

Figure 10. Time-dependent evolution of the luminosities (upper row) and neutrino fluences (lower row) for model M-IR. For details, see the caption of Figure 4; the additional contribution from the IR photon interactions is the orange dashed–dotted curve in the lower row.

streaming escape-dominated at the highest energies, which means that $L_{p,\mathrm{cal}}^{\mathrm{eff}} \propto N_p \simeq J_p t_{\mathrm{fs}} \propto L_p$ from Equation (3); the reason is the more compact production region, leading to higher escape rates. Since the target photon density is relatively constant over a wide time window and the neutrino luminosity is $\propto L_{p,\mathrm{cal}}^{\mathrm{eff}} \times L_{\mathrm{IR}}$, it follows L_p to leading order for this TDE.

The neutrino fluences in the lower row (see also Figure 8, right table) are more comparable to M-X rather than to M-OUV. The predicted numbers of events lie within the expected ranges in Table 1 for $\varepsilon_{\mathrm{diss}} \gtrsim 0.1$. The peaks of the fluences are all dominated by the IR interactions (orange dashed–dotted curves) because of the high enough proton energies, but OUV interactions (blue dotted curves) contribute significantly in all cases. This is unavoidable, since IR and OUV are directly connected, which means that a part of the OUV luminosity is re-processed into the IR dust echo—and consequently the OUV interactions (which also have a lower threshold) cannot be avoided. The predicted neutrino energies are significantly higher than the most likely energies (black arrows), which is the biggest limitation of model M-IR.

Discussion. Model M-IR provides the best description of the neutrino time delay due to the time evolution of the dust echo target, with the exception of AT2019dsg. The neutrino delay description could be improved somewhat by a larger value of R (because the protons interact more slowly), at the expense of the overall neutrino production efficiency. Therefore, there is no good trade-off between time delay and neutrino fluence for AT2019dsg. Major disadvantages of model M-IR are the predicted neutrino energies peaking at very high values (which are significantly above the detected energies), and the relatively low predicted neutrino fluences.

The location of the accelerator $R_{\mathrm{acc}} < R_{\mathrm{dust}} \simeq R$ can be, in principle, anywhere in the isotropization region. However, we know from the discussion of Equation (7) that the confinement condition already indicates that $R_{\mathrm{acc}} \gtrsim 3 \, 10^{16}$ cm for $E_{p,\mathrm{max}} \simeq$ EeV and $B = 0.1$ G, which points toward $R_{\mathrm{acc}} \sim R$; a wind or outflow could serve as accelerator, which is however challenged by the required large $\varepsilon_{\mathrm{diss}}$. The acceleration may also occur in more compact regions in the core (corona, disk) or a jet with larger values of B; especially in the case of the core models, additional contributions would add to the neutrino signal from the more compact regions, which we do not describe here.

We would like to note that the model M-IR could be connected with the origin of the UHECRs (which is why we refer to "ultra-high" proton energies in this section). Depending on nuclear disintegration and air shower models, a maximum rigidity $R_{\mathrm{max}} \simeq (1.4–3.5) \, 10^9$ GV was found in Heinze et al. (2019) to describe data from the Pierre Auger Observatory (Aab et al. 2017) in the rigidity-dependent maximal energy model in multidimensional parameter space fit. This range is sufficiently close to the assumption made for protons here $E_{p,\mathrm{max}} = 5 \, 10^9$ GeV, which means that TDEs similar to the ones discussed in this work could also be the sources of the UHECR protons. For heavier nuclear compositions, which are needed to describe UHECR data, the neutrino fluence is expected to be similar for an E^{-2} cosmic-ray acceleration spectrum (see Morejon et al. 2019 for the dependence of $A\gamma$ interactions on the mass number) as long as the source is optically thin to nuclear disintegration at the highest energies; see Biehl et al. (2018b) and Morejon et al. (2019) for corresponding examples. Of course, the nuclear composition

might be motivated by appropriate progenitor disruptions, such as ONe or CO white dwarfs. Concerning the energy output in UHECRs, we know that the energy in nonthermal protons per TDE is $E_p \simeq \varepsilon_{\text{diss}} \int \dot{M} dt \simeq 0.1 M_\star$ in our model for the optimistic $\varepsilon_{\text{diss}} = 0.2$, where $M_\star$ is given in Table 1. Taking into account the bolometric correction (only protons at the highest energies are relevant here) and that only a fraction of UHECR protons escape (see, e.g., Heinze et al. 2020 for a corresponding discussion in GRBs), one may estimate that $E_p^{\text{esc}} \lesssim 0.01 M_\star$ can be re-processed into nonthermal protons at the highest energies per TDE; for a solar-mass star, that is about $2 \, 10^{52}$ erg. This would require a local white dwarf disruption rate of about $5 \, \text{Gpc}^{-3} \, \text{yr}^{-1}$ to match a local injection rate of 10^{44} erg Mpc^{-3} yr^{-1}—which has been perceived as too high in the literature (see, e.g., discussion in Biehl et al. 2018b). While more recent observations have found much higher local rates, $500 \, \text{Gpc}^{-3} \, \text{yr}^{-1}$ (Tanikawa et al. 2022), it is critical here how the population extends to large SMBH masses (as the UHECR output in our model scales with $M \propto L_{\text{edd}}$); a detailed population model is beyond the scope of this study. Another possibility could be that material from the preexisting AGNs is injected into the acceleration process, which would impact both energy budget and UHECR composition.

6. Predicted Diffuse Neutrino Fluxes

Using the results in the previous sections, we have computed the expected diffuse flux of neutrinos from TDEs, following the method outlined in Lunardini & Winter (2017). The neutrino flux of a given flavor α—differential in energy, time, area, and solid angle—is given by:

$$\Phi_\alpha(E) = \frac{\eta c}{4\pi H_0} \int_{M_{\text{min}}}^{M_{\text{max}}} dM \int_0^{z_{\text{max}}} dz$$
$$\times \frac{\dot{\rho}(z, M) Q_\alpha(E(1+z), M)}{\sqrt{\Omega_M (1+z)^3 + \Omega_\Lambda}}, \qquad (20)$$

where $\dot{\rho}(z, M)$ is the cosmological rate of TDEs differential in redshift and SMBH mass (obtained following Shankar et al. 2009; Stone & Metzger 2016; Kochanek 2016); see also Holoien et al. 2016; van Velzen 2018; Hung et al. 2018 for rate measurements). The function Q_α is the number of neutrinos emitted per unit energy in the SMBH frame (inclusive of neutrino flavor oscillations in a vacuum) for a single TDE having an SMBH of mass M, taken from our results of Sections 3, 4, and 5, respectively, for each of the three models. It corresponds to the quantity J in Equation (3) integrated over the volume of the radiation zone and over the emission time. The quantity $E' = E(1+z)$ is the neutrino energy in the SMBH frame; E is the energy observed at Earth. Here η is the fraction of TDEs where the neutrino production mechanism is active and efficient. Equation (20) also includes the speed of light, c, the Hubble constant, H_0, and the fractions of cosmic energy density in dark matter and dark energy, $\Omega_M \simeq 0.3$, and $\Omega_\Lambda \simeq 0.7$.

In computing the expression in Equation (20), $z_{\text{max}} = 6$ is used, its value influences the result only weakly. We also choose $M_{\text{min}} = 2 \, 10^6 \, M_\odot$ and $M_{\text{max}} = 5 \, 10^7 M_\odot$, which is justified by the estimated masses in Table 1, when considering their uncertainty (at least a factor of 2). The upper cutoff M_{max}

is also expected because tidal disruption becomes increasingly inefficient for increasing M (see, e.g., Kochanek 2016).

The integration in M is approximated by a discrete sum over three mass bins. Specifically, we work under the assumption that the entire TDE population is represented, although roughly, by the three neutrino-detected TDEs, each of which correspond to a different value of M. For each model, our benchmark scenario assumes that the three neutrino spectra found for AT2019dsg, AT2019fdr, and AT2019aalc contribute equally to the diffuse flux, so they are assigned equal weights: $(w_1, w_2, w_3) = (1/3, 1/3, 1/3)$. This choice is the best inference that can be obtained from observations. It is also plausible theoretically: considering the three mass values in Table 1 with uncertainties, it is possible that the observed TDEs may fall in the mass bins $M/M_\odot = [2 \, 10^6, 4 \, 10^6]$, $[4 \, 10^6, 10^7]$, $[10^7, 4 \, 10^7]$, which correspond to equal TDE rates for our chosen $\dot{\rho}(z, M)$. To describe the uncertainty on the neutrino spectrum and normalization, we also vary over all of the possible weights (w_1, w_2, w_3), thus obtaining an envelope of curves with the purpose of quantifying the uncertainty of how representative each TDE is for the full population.

The resulting $\nu_\mu + \bar{\nu}_\mu$ flux is shown in Figure 11 for the benchmark case (central curve) as well as the varying weights one (shaded area). Also shown are the corresponding flux measurements from cascade-like (Aartsen et al. 2020b) and track-like (Abbasi et al. 2022) events at IceCube. In the figure, the fraction of neutrino-emitting TDEs, $\eta \lesssim 1$, has been adjusted to reproduce the data; chosen values are

$$\eta = \begin{cases} 10^{-0.5}, 10^{-2.3}, 10^{-2.0} & \text{for } \varepsilon_{\text{diss}} = 0.2 \\ 10^{0.1}, 10^{-1.7}, 10^{-1.4} & \text{for } \varepsilon_{\text{diss}} = 0.05 \end{cases}, \qquad (21)$$

where the three values listed in each case refer to M-X, M-OUV, and M-IR, respectively. Here we have used the degeneracy between η and the dissipation efficiency $\varepsilon_{\text{diss}}$: we observe that $Q_\alpha(E(1+z), M) \propto \varepsilon_{\text{diss}}$, and therefore $\Phi_\alpha \propto \eta \, \varepsilon_{\text{diss}}$. This implies that the data can be reproduced with more moderate requirements for the dissipation efficiency into nonthermal protons over the whole TDE population, at the expense of a larger fraction of neutrino-emitting TDEs (which could be as large as one). There is also a degeneracy with M_{min}: due to the negative evolution of the TDE rate with mass, Φ_α increases when lowering M_{min}. For $M_{\text{min}} \sim 10^5 M_\odot$, an order of magnitude increase is expected with respect to our results (see, e.g., Lunardini & Winter 2017), thus leading to lower requirements for $\eta \varepsilon_{\text{diss}}$. From Figure 11 and the comparison with the measured spectrum, we conclude that, for M-OUV and M-IR, TDEs cannot be the main contributors to the astrophysical flux observed by IceCube, but they may significantly contribute at the highest energies $E \gtrsim 1$ PeV. In contrast, for M-X, the predicted spectrum reproduces the data over 3 orders of magnitude of energy. We note that this conclusion depends strongly on the spectrum weights w_i; in the case where the spectrum for AT2019dsg (which is more suppressed at low energy compared to the others; see Figure 4) carries a large weight, the observed flux at $E \lesssim 0.1$ PeV cannot be accounted for by TDEs.

It is an interesting question of whether the chosen values of η are roughly consistent with the number of neutrino-TDE associations that have been found through neutrino follow-up
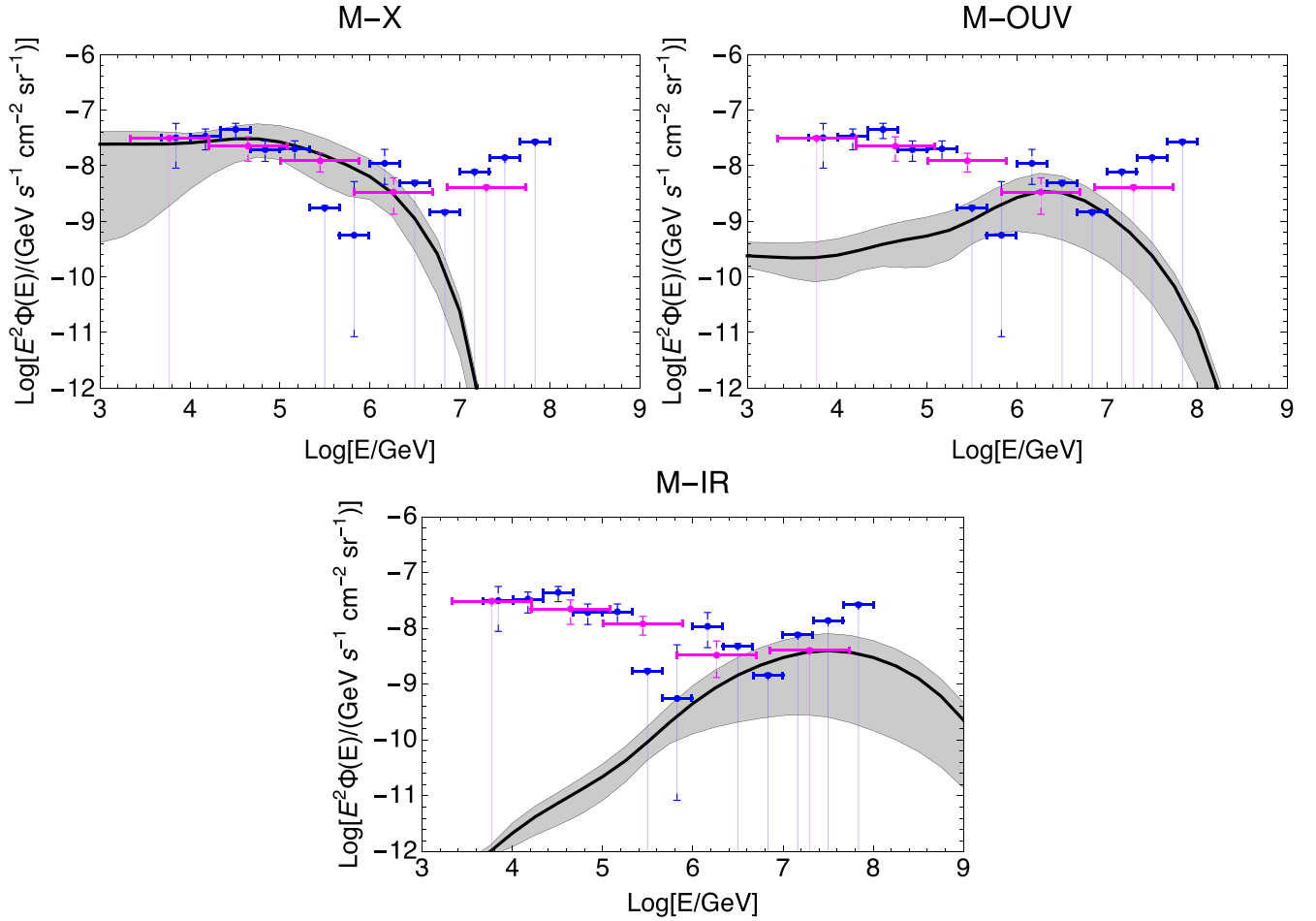
Figure 11. $\nu_\mu + \bar{\nu}_\mu$ diffuse fluxes for the three models, for the case where the three single-TDE spectra contribute with equal weights (solid curves) or arbitrary weights are allowed (shaded areas). The fractions of contributing TDEs have been set to the values given in Equation (21) to reproduce the observed diffuse flux. Data points represent the IceCube measurements from cascades (Aartsen et al. 2020b; blue, data with narrower energy bins) and tracks (Abbasi et al. 2022; magenta, data with larger energy bins).

programs. If we consider the rate of these associations to be about one per year; generically one expects $\eta \simeq 1\,\mathrm{yr}^{-1}/(\dot{N}\,N_{\mathrm{GFU}})$, where $\dot{N}$ is the yearly rate of TDEs that can—at least in principle —be found by standalone or follow-up observations ("observable" TDEs), N_{GFU} is the predicted neutrino event rate from our models, and we assume (optimistically) that most neutrino events are followed up. An estimate of $\dot{N}$ can be obtained by integrating $\dot{\rho}(z, M)$ in the quoted mass range, and up to a redshift that roughly matches the reach of current instruments. We obtain $\dot{N} \simeq 10^4\,\mathrm{yr}^{-1}$ for $z < 0.3$, and $\dot{N} \simeq 400\,\mathrm{yr}^{-1}$ for $z < 0.1$, which serve as the range of uncertainty for this estimate from the instrument redshift threshold only.[20] Taking the average values for N_{GFU} over the three TDEs (see Figures 2, 5, 8, right tables), one would expect the following ranges for η: for $\varepsilon_{\mathrm{diss}} = 0.2$, the intervals $\eta \in [10^{-2.6}, 10^{-1.2}]$, $[10^{-3.7}, 10^{-2.3}]$, and $[10^{-2.4}, 10^{-1.0}]$ for M-X, M-OUV, and M-IR, respectively, and for $\varepsilon_{\mathrm{diss}} = 0.05$ the intervals $\eta \in [10^{-2.0}, 10^{-0.6}]$, $[10^{-3.1}, 10^{-1.7}]$, and $[10^{-1.8}, 10^{-0.4}]$. Comparing these expectations to reproduce the number of TDE associations with the numbers to reproduce

data in the respective energy ranges in Equation (21), we can estimate the expected contribution to the diffuse flux from the ratio of these numbers: 0.8%–20%, $\gtrsim 4\%$, and $\gtrsim 38\%$ for M-X, M-OUV, and M-IR, respectively, where the dependence on $\varepsilon_{\mathrm{diss}}$ cancels. This means that the diffuse neutrino flux for M-X shown in Figure 11 would probably lead to too many neutrino neutrino-TDE associations, while the other two are plausible. For comparison, a range between 5% and 59% of the diffuse flux is given in Bartos et al. (2021) at the 90% CL; this range is roughly consistent with our estimates, given the systematic uncertainties. Note that the number of astronomically (in the electromagnetic bands) observable neutrino-emitting TDEs is given by $\eta \cdot \dot{N}$ in this approach, which ranges between 2 and 40 per year (8 and 160 per year) for $\dot{N} \simeq 400\,\mathrm{yr}^{-1}$ and $\varepsilon_{\mathrm{diss}} = 0.2$ (0.05). These ranges are roughly consistent with the number of interesting TDE candidates found in van Velzen et al. (2021a) selected by the strength of the dust echoes, which supports the hypothesis that the neutrino-emitting TDEs and the TDEs with strong dust echoes could indeed be the same populations. It is also interesting to note that, after the discovery of the jetted TDE AT2022cmc, the recently derived fraction of TDEs having jets in the percent range (Andreoni et al. 2022) is consistent with our estimated ranges for η, which also means that the neutrino-emitting TDEs and jetted TDEs could be the same populations; see Appendix A for details.

---

[20] Our results for $\dot{N}$ imply that the number of *observable* TDEs per year is much larger than the number of actually *observed* TDEs (perhaps a few tens) per year. The difference between the two rates is explained by the duty cycle and field of view of the instruments, and the difficulty to classify events as TDEs—even the nearby ones—because of the instrument threshold.

Table 2
Qualitative Comparison of Different Models Regarding Different Aspects

Model Criterion	M-X	M-OUV	M-IR
Accelerator: Scale comparison	$R \simeq R_{\rm acc} \gtrsim R_{\rm BB}$	$R \simeq R_{\rm BB} \gtrsim R_{\rm acc}$	$R \simeq R_{\rm dust} \gtrsim R_{\rm acc}$
Required $\varepsilon_{\rm diss}$	$\gtrsim 0.1$–0.2	$\gtrsim 0.03$	$\gtrsim 0.1$
Wind/outflow models	Challenged by $\varepsilon_{\rm diss}$, $t_{\rm ad}$	Unlikely ($R_{\rm acc} > R$, $\eta_{\rm acc}$)	Challenged by $\varepsilon_{\rm diss}$
Off-axis jet	Yes	No (no isotropization in R)	Yes
Core models (disk, corona)	Not described	Yes, but $E_{p,\rm max}$?	Not fully described
Main targets	X-rays, protons	Optical-UV blackbody	IR from dust echo
Observational evidence/correlation	X-ray signals	High $L_{\rm BB}$	Dust echoes
Origin of neutrino time delay	Diffusion (high B)	Unrelated to size of system	Dust echo travel times
Description neutrino time delay	Intermediate	Poor	**Good**
Neutrino event rate	Low	**Intermediate-High**	Low
Required $E_{p,\rm max}$	**Moderate**	Intermediate	Ultra-high
Neutrino energy	**Matches**	Somewhat high	Very high
Neutrino spectral time evolution	**Matches**	Right direction	Wrong direction
Diffuse flux spectral shape	**Matches**	High E only	Highest E only
Diffuse flux contribution	0.8%–20%	$\gtrsim 4\%$ (high E only)	$\gtrsim 38\%$ (highest E only)

Note. Best matches are boldfaced.

7. Comparison and Discussion

Let us take a comparative look at the three models we have proposed; a first question that arises is which model, if any, is favored by observations. We give a qualitative comparison of the three models in Table 2. From the table, it appears that at present there is no clear preference for a single model. In terms of neutrino signal, M-X describes the neutrino energy very well, and the required $E_{p,\rm max}$ is moderate; M-OUV can most easily describe the expected neutrino fluence, and therefore has the best requirement for the transfer efficiency of accretion power into nonthermal protons; M-IR describes the neutrino time delay best. Major drawbacks are the poor time delay description in model M-OUV, and the ultra-high proton and neutrino energies in model M-IR, so that, overall M-X seems to be a very attractive choice. However, M-X can only describe up to 20% of the diffuse neutrino flux as estimated from the neutrino-TDE associations, and the neutrino signal from AT2019aalc may not be driven by X-rays due to the low observed X-ray luminosity. The best candidate for the acceleration region might be an off-axis jet for model M-X, an accelerator in the core for M-OUV (if high enough proton energies can be reached), and an outflow, wind or jet for M-IR.

As was noted before, all three neutrino-TDE associations require SMBH masses around $10^7 \, M_\odot$, which is high compared to the mean of the observed TDE population. Our models are roughly consistent with this scaling with M. Indeed, for M-OUV, both the proton injection rate L_p (by construction) and the BB luminosity (from observations/theoretical expectations; see Table 1) are proportional to $L_{\rm Edd} \propto M$, which means that one expects $L_\nu \propto L_p \times \tau_{p\gamma} \propto L_p \times L_{\rm BB} \times T^{-1} \propto L_p \times L_{\rm BB}^{3/4} \propto M^{7/4}$ (where Equation (15) and the Stefan–Bolzmann law were used) in the $p\gamma$ optically thin case, saturating to $L_\nu \propto L_p \propto M$ in the optically thick case (where all proton energy is effectively transferred into neutrinos)—which means that the neutrino-TDE associations will be likely dominated by the upper end of the SMBH range even if the differential TDE rate scales as $M^{-1.6}$; see discussion in Lunardini & Winter (2017). For M-IR, the same argument holds, since the intensity of the dust echo is proportional to the one in OUV. Instead,

predicting a scaling with M for M-X is more difficult. For AT2019aalc, the neutrino production is dominated by pp interactions, for which the same scaling of the other models applies. For the other two TDEs, one could apply the prediction by Mummery (2021; see also Mummery & Balbus 2020) that L_X should be nearly constant over a wide mass range, leading to $L_\nu \propto M$ even in the optically thin case and to the same qualitative agreement with the three measured SMBH masses (note however, that the X-ray spectrum would have a nontrivial dependence on M, which would affect the neutrino spectrum; Mummery 2021).

To elaborate on the consistency between the models and detected neutrino events, let us examine the time-dependent evolution of the neutrino spectrum, which could be complicated. Especially if different target photon spectra contribute to the neutrino production, we have seen that the interaction rates will be very different for these; this means that, e.g., neutrinos from OUV interactions will be closely following the proton injection because the system is optically thick, whereas neutrinos from X-ray and IR interactions are intrinsically produced later due to the calorimetric behavior. Therefore, there is a connection between the expected neutrino energy and the time delay. We illustrate this in Figure 12 for the three different models for the example of AT2019dsg, where the time evolution of the neutrino spectrum is shown (from red–early to blue–late, black curves refer to the time of the neutrino emission). For M-X, the early spectrum from OUV interactions peaks at higher energies than the spectrum at the actual time of the neutrino emission; in all cases, the spectrum matches well. For M-OUV, the overall neutrino emission will be dominated by earlier times and relatively high neutrino energies within the possible range, whereas at the time of neutrino emission the spectrum is relatively flat in the expected (gray-shaded) range; the spectral evolution thus is in the right direction. For M-IR, it is actually the early emission (from the OUV target) that peaks closer to the observed neutrino energy, whereas at the time of the neutrino emission, the spectrum peaks at too high energies; so, the temporal evolution of the spectrum actually increases the tension with observations. These qualitative observations are also listed in our Table 2.
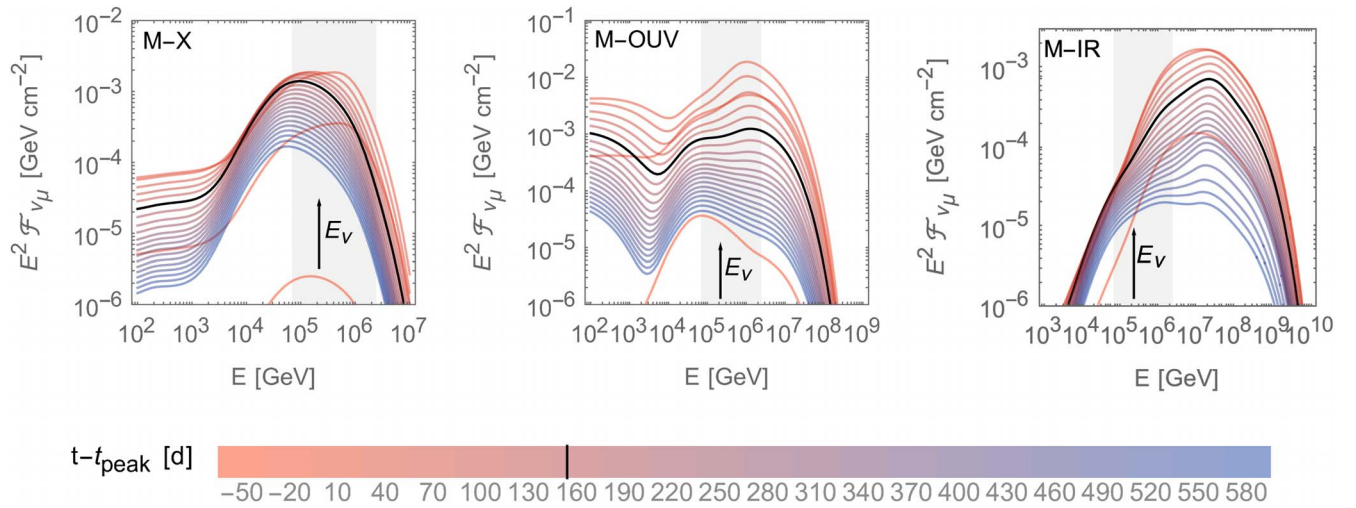
Figure 12. Time evolution of the emitted neutrino fluence as a function of the observed energies for the three different models for AT2019dsg compared. Note that the individual shown fluences for the time slices add up to the total fluence. Black curves are closest to the actual neutrino emission, and likely neutrino energies are marked as described in the caption of Figure 4.

At a more detailed level, one could wonder which of the three observed TDEs is best described by our models. We find that for AT2019aalc the neutrino fluence and time delay are well reproduced because of its relatively large SMBH mass (resulting in higher luminosities), low redshift, and slower decline of the BB luminosity. AT2019dsg on the other hand, has a faster declining BB luminosity, which makes the description of the neutrino time delay more difficult because nonthermal proton injection will peak early. While AT2019fdr exhibits high neutrino luminosities in the SMBH frame, the neutrino fluence at Earth is suppressed due to the high redshift. Interestingly, for AT2019aalc very high point-source event rates are found for models M-X and M-OUV, which leads to the conclusion that (subject to Poissonian fluctuations) the source could have even been independently found as neutrino point source for large enough $\varepsilon_{\rm diss}$; instead, for the other two TDEs, the Eddington bias argument has to be invoked.

High neutrino fluences, however, imply that gamma-rays from accompanying neutral pion decays will be abundantly produced, which means that gamma-ray observations may constrain the predicted neutrino fluxes. The electromagnetic cascade triggered by gamma-gamma pair production depends on the time evolution of the photon density across the spectrum, potentially including photon components not included in our models. In the most conservative optically thick (to $\tau_{\gamma\gamma}$) case, the cascaded gamma-ray flux is expected to be at the level of the neutrino flux typically peaking below the pair production threshold, which is about 5 GeV if X-rays are abundant enough, and 500 GeV otherwise (such as for AT2019aalc). If one compares the neutrino fluxes to the gamma-ray limits in van Velzen et al. (2021a), one finds rough consistency for most TDEs and models, but the expected gamma-ray fluxes are potentially observable in some cases, especially for M-OUV (all TDEs) and AT2019dsg (all models). While detailed models are beyond the scope of this study, one may expect that $\varepsilon_{\rm diss}$ could be constrained.

Finally, let us comment on how our proposed mechanisms could apply to other classes of sources. A natural comparison is with AGNs. In van Velzen et al. (2021a) it is concluded that AGNs must be less "efficient particle accelerators" than TDEs

because, in the electromagnetic channel, steady AGN emission outshines that of TDEs at least by 2 orders of magnitude—and the same is not observed in neutrinos, despite the similarities between AGNs and TDEs (for example, all AGNs have large regions with hot dust that could produce targets for neutrino production). We anticipate that the comparison is in fact more complex than an electromagnetic output comparison. First of all, the acceleration of protons to such high energies may only take place in components present in one source class, such as the debris stream-return stream collisions in TDEs, which means that the accelerator may simply not be present in AGNs (or have very different properties). Second, since the neutrino luminosity (for $p\gamma$ interactions in the optically thin case) scales as $L_\nu \propto L_p \times \tau_{p\gamma}$, where $\tau_{p\gamma}$ strongly depends on the size of the radiation zone, efficient proton acceleration (powering L_p) is only one part of the problem, the other is how efficiently these nonthermal protons (if they exist) can transfer energy into neutrinos (magnitude of $\tau_{p\gamma}$). To illustrate that, let us consider jets, which could be realized in both source classes. It is known that AGN blazars (jets pointing toward us) suffer from low $\tau_{p\gamma}$ for parameters required to describe the spectral energy distribution (see, e.g., Gao et al. 2019 for TXS 0506+056, and Oikonomou 2022 for a more general discussion). This needs to be compensated by a correspondingly larger L_p, i.e., large baryonic loading often related to super-Eddington accretion rates, which are sometimes perceived to be unrealistic. Our models are qualitatively different: $\tau_{p\gamma}^{\rm cal}$ in the relevant radiation zone is comparatively large (which means that TDEs are indeed efficient neutrino sources), and hence the required baryonic loading (if defined as energy injected into protons versus BB) of about 30–100 (even for the large $\varepsilon_{\rm diss} = 0.2$) is more comparable to expectations for GRBs as UHECR sources than AGNs (see, e.g., Heinze et al. 2020). This means that TDEs may (i) host more efficient proton-accelerating sites, (ii) have more compact radiation zones, or (iii) support a more effective proton confinement than AGNs. That, on the other hand, implies that models clearly inspired by AGN physics, such as the corona core model (Murase et al. 2020b), are challenged by this argument—and must require

very different parameters in AGNs and TDEs to explain that observed difference.

8. Summary and Conclusions

We have studied fully time-dependent quasi-isotropic neutrino production models for the three TDEs associated with high-energy astrophysical neutrinos, postulating that the observed neutrino time delays with respect to the BB peak come from the physical size of the post-disruption system, such as confinement of protons in magnetic fields over a large enough region, or propagation time delays. We have pointed out that the dominant photon target for proton interactions depends on the available maximal proton energy provided by the acceleration region; we have not specified the accelerator explicitly, but instead have parameterized it by the maximal proton energy and proton injection luminosity of a nonthermal spectrum (with power-law index two); examples could be off-axis jets, hidden winds, shocks from outflow-environment interactions, or stream-stream collisions. For one of the models (M-OUV), the disk or corona could be acceleration sites, too, if high enough proton energies can be reached.

We have focused on observations common to the three TDEs, which, apart from the neutrino time delays, are: (a) X-ray signals, (b) relatively high SMBH masses, and, correspondingly, also relatively high BB luminosities, and (c) strong dust echoes. Our models consequently have adopted X-ray (model M-X), optical-UV BB (model M-OUV), and IR (model M-IR) photons as main interaction targets, selected by the maximally available proton energy, targeting the question of what the smoking gun signature for the neutrino production actually is. A qualitative comparison is given in Table 2. Model M-X describes the observed neutrino energies and time delays well due to the confinement of moderate-energy protons if the unobscured X-ray luminosity is roughly constant as a function of time; model M-OUV describes the highest neutrino event rates at the expense of small neutrino time delays; model M-IR provides a good description of the neutrino time delays because of the correlation with dust echoes with similar delays, and it may actually power the diffuse neutrino flux at the highest energies, at the expense of very high proton and neutrino energies. Note that TDEs may also be the sources of UHECRs if model M-IR can be established, but a more quantitative approach requires further study.

Since our models predicts a neutrino luminosity roughly scaling as $L_\nu \propto M^{(1-2)}$, it not surprising that the observed neutrino-TDE associations involve SMBHs that are more massive than the mean of the observed TDE population. From that perspective, the newly found TDE AT2019aalc, which was associated with the highest SMBH mass M (subject to large uncertainties) and the lowest redshift, is expected to produce the highest neutrino fluence, which we have seen in all models. In fact, in two models, the event number using the PS effective area was larger than that if the dissipation efficiency $\varepsilon_{\mathrm{diss}}$ is high, which means that this source could be seen in (transient) multiplet or PS searches, whereas the detection of the other two was predicted to be a matter of chance (from a larger sample of sources with low predicted event rates each, invoking the Eddington bias). Note, however, that the information on AT2019aalc is sparse, which means that there are larger uncertainties (than for the other two TDEs). Especially in this case, the search for/comparison to additional electromagnetic signatures, e.g., from secondaries produced in

the photoion production, which may also follow the time dependence of the neutrino spectra, could be interesting.

A major limitation of our approach is the relatively large required dissipation efficiencies $\varepsilon_{\mathrm{diss}} \gg 0.05$ from mass accretion rate into nonthermal protons for the individual TDE models M-X and M-IR, whereas M-OUV can tolerate smaller efficiencies due to the high BB target photon density. For example, the requirement of high $\varepsilon_{\mathrm{diss}}$ poses a challenge to outflow models if $v \lesssim 0.5\,c$, and to off-axis jetted models if the dissipation efficiency of kinetic energy into nonthermal particles (e.g., in internal shocks) is less than about 25%. Our diffuse flux computation has demonstrated that the average $\varepsilon_{\mathrm{diss}}$ of the whole population could be lower, at the expense of a larger fraction of neutrino-emitting TDEs. As far as the origin of the neutrino time delays is concerned, its description has been especially challenging by our assumption that the nonthermal proton injection follows the mass accretion rate; we have proposed a calorimetric approach paired with a relatively low (free-streaming) optical thickness (models M-X and M-IR), or paired with time-delayed target photons (dust echo model M-IR). Note that the magnetic confinement of protons has the advantage that protons emitted in different directions isotropize, such as from off-jets. Other possible reasons for the neutrino time delays include a time evolution of the proton injection different from the mass accretion rate, or a transition of the disk state in core models.

We conclude that a decision of the neutrino production model based on the available information cannot be made; future observations will show if X-ray signals are associated with neutrinos from TDEs (points toward M-X), or if dust echoes are observed (pointing toward M-IR); in both of these cases, time delays of the neutrinos are expected as well. If, on the other hand, BB-luminous TDEs with neutrinos close to the BB peak are found, M-OUV will be preferred. Note that other signatures initially gauged interesting for AT2019dsg (Stein et al. 2021b), such as the outflow and radio signals, may actually be of secondary importance for the neutrino production in the light of AT2019fdr and AT2019aalc. Important clues will also come from the observed neutrino energies, which will have to be scrutinized with more realistic spectra; minor correlations between neutrino arrival time and neutrino energy are also expected in the models. Depending on the scenario, protons, such as in an outflow or the debris stream, may also be a target for neutrino production; in our cases, these have not affected the qualitative conclusions, but may help to describe the soft diffuse neutrino flux at the low energies. A more challenging question may be of the origin of the accelerated protons: can these be associated with other nonthermal signatures in the electromagnetic spectrum that will allow for an identification of the acceleration region, or will the origin of the nonthermal protons remain a mystery?

Appendix A
Discussion of Jetted Models (On-axis, Off-axis)

The isotropic models presented in this study are very different from jetted models (with jets pointed toward us, or

slightly off-axis); see Winter & Lunardini (2021), Liu et al. (2020; AT2019dsg), and Reusch et al. (2022; AT2019fdr). The major limitation of the quasi-isotropic emission models is the very large fraction of energy has to go into nonthermal protons compared to models with a collimated emission; see Winter & Lunardini (2022) for a discussion. In jetted models, $\varepsilon_{\rm Comp} \simeq 20\%$ of the total accretion power is assumed to go into the jet (Dai et al. 2018), and the transfer efficiency from kinetic energy to nonthermal radiation $\varepsilon_{\rm NT}$ can, depending on the outflow model, be around 10%–40% (see, e.g., Rudolph et al. 2020; Heinze et al. 2020). Using $\varepsilon_{\rm NT} \simeq 25\%$ results in an overall fraction $\varepsilon_{\rm diss} \simeq 0.05$ into nonthermal protons—which is at the lower end of the range proposed here; high isotropic-equivalent proton luminosities are then reached by relativistic beaming. Note, however, that we use the most conservative $E_{p,\rm min} \simeq 1$ GeV in all cases, which means that a large fraction of nonthermal protons cannot interact by $p\gamma$ interactions because they are below threshold; increasing $E_{p,\rm min}$ or harder acceleration spectra would reduce the efficiency challenge for the individually observed TDEs. A big question for jetted models has been the nonobservation of nonthermal internal radiation, and the interpretation of the radio observations for AT2019dsg, which indicate that the jet may have been unusually narrow ($\theta \ll 1°$; Cendes et al. 2021). This immediately raises the question why the neutrino-TDE associations can be so abundant, as most jetted TDEs would not be seen in our direction for such a narrow jet.

Strongly off-axis jets acting as proton accelerators would be a possible solution to the puzzle, as the particle acceleration itself is known to work efficiently in astrophysical jets. In this case, escaping nonthermal protons need to escape on the scale within our radiation zone, and to be trapped within the calorimeter and isotropize—which is in principle possible in our calorimetric models M-X and M-IR (see Figures 3 and 9: energy ranges where $t_{p,\rm esc}^{-1} < t_{\rm fs}^{-1}$). Similar ideas have been proposed on different scales (see, e.g., discussions in Fang & Murase 2018; Rodrigues et al. 2021). Note that here the cosmic-ray escape mechanism from the jet is also critical: for example, neutron escape does not contribute as neutrons cannot be magnetically confined, and advective escape may not work at the relatively small scales R proposed for M-X, whereas direct or diffusive escape of high-energy protons could work (Baerwald et al. 2013), i.e., of protons for which the Larmor radius reaches the size of the accelerator. The advantage of an off-axis jet is that the jet can serve as proton accelerator, while other radiation signatures of the jet are not expected or too weak if the viewing angle is large enough; in addition, all TDEs with jets would serve as neutrino sources (not only the ones pointing toward us), whereas the chance coincidence for a jet to point into our direction is at the percent level (Andreoni et al. 2022). Since the required nonthermal proton luminosity is comparable to the typically expected physical (kinetic) jet luminosity, the jets would have to be very efficient to transfer kinetic energy into nonthermal particles for the three TDEs discussed here (and the jet collimation cannot be used to increase the isotropic-equivalent energy for an off-axis jet). For the diffuse flux, note that not all TDEs are expected to produce relativistic jets; fractions of jetted TDEs of $\eta \simeq 0.1$, as assumed in Lunardini & Winter (2017), or, more conservatively, $\eta \simeq 0.01$, as inferred in Andreoni et al. (2022), are compatible with the η-ranges derived in Section 6 from the number of neutrino-TDE associations for M-X and M-IR (for $\varepsilon_{\rm diss} \simeq 0.05$), which means that the neutrino-emitting TDEs and jetted TDEs could be the same population.

Appendix B
On the Effect of Adiabatic Cooling

Since the adiabatic expansion rate depends on the nature of the radiation zone and its relationship to the accelerator, we do not include it in the main text, but we discuss its effects on the neutrino fluence here. Adiabatic cooling can limit the calorimetric behavior of the system as the confined protons may lose energy by the expansion of the radiation zone faster than they can interact. Neglecting adiabatic cooling is justified if the radiation zone is stable enough such that the adiabatic cooling rate is $t_{\rm ad}^{-1} \lesssim t_{p\gamma}^{-1}$ (beyond the $p\gamma$ threshold). Fits of the BB radius, which typically decreases over time (van Velzen et al. 2021b), may support a stable production region. If, however, a nonrelativistic outflow is indicative for the expansion of the system, then $t_{\rm ad}^{-1}$ is given by $t_{\rm ad}^{-1} \simeq 4/3 \cdot v/R \sim v/R \simeq 0.1\, t_{\rm fs}^{-1}$ to $0.5\, t_{\rm fs}^{-1}$ can be quite substantial for some models; see below.

First of all, note that adiabatic cooling affects the models differently. For model M-OUV, the radiation zone is optically thick, and adiabatic cooling will hardly have an effect on the (dominant) contribution from OUV interactions; see Figure 6 ($t_{\rm ad}^{-1} < t_{\rm fs}^{-1} < t_{p\gamma}^{-1}$ here). For model M-IR, $t_{\rm ad}^{-1}$ is, because of the
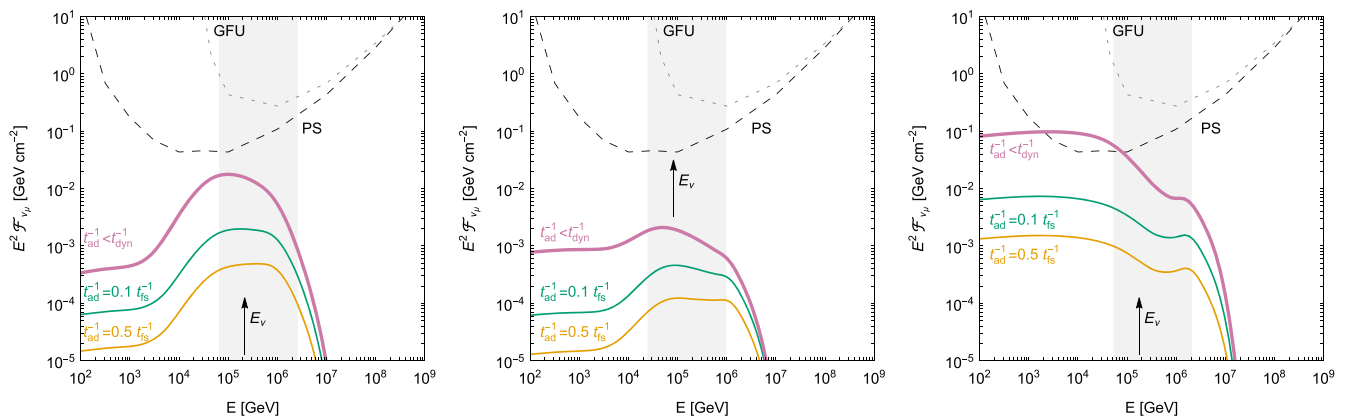

Figure 13. Neutrino fluences for model M-X for AT2019dsg, AT2019fdr, and AT2019aalc in the left, middle, and right panels, respectively. In each panel, the different curves correspond to different adiabatic cooling rates, as given in the legends. Of these, the highest (reddish-purple) curve corresponds to Figure 4 (see also that figure caption for details).

large radiation zone, potentially close to $t_{\rm dyn}^{-1}$ (for $t_{\rm ad}^{-1} \sim 0.1\, t_{\rm fs}^{-1}$); in either case, $t_{\rm ad}^{-1} \lesssim t_{\rm p\gamma}^{-1}$ here (see Figure 9), so the effects of adiabatic cooling are expected to be small. We are therefore mostly targeting model M-X (see Figure 3), for which the adiabatic cooling rate could be potentially higher than the Bethe–Heitler cooling and photohadronic interaction rates, which can reduce the expected neutrino fluences.

In Figure 13, we show the impact of adiabatic cooling on the neutrino fluences for model M-X for the three TDEs considered in this work and different adiabatic cooling rates corresponding to outflow models with $v = 0.1\, c$ and $0.5\, c$ (leading to $t_{\rm ad}^{-1} \simeq 0.1\, t_{\rm fs}^{-1}$ and $0.5\, t_{\rm fs}^{-1}$, respectively). For comparison, the curves for $t_{\rm ad}^{-1} < t_{\rm dyn}^{-1}$ (which is slower than the interaction rates, which means that adiabatic cooling is subdominant) are shown as well. As can be seen from the figure, the adiabatic cooling can suppress the neutrino fluence substantially because it may dominate the cooling of the protons. We consequently note that especially for model M-X, a stable radiation zone is required. Since $R \simeq R_{\rm acc}$ for that model, the acceleration zone should also not expand substantially (if it is identical to the radiation zone) or should release the protons at $R_{\rm acc}$ into a static radiation zone with $R \simeq$ constant. We speculate that this could be, e.g., a sufficiently slow nonrelativistic outflow with $v < 0.1\, c$, outflow–cloud interactions in a specific distance $R_{\rm acc}$ from the SMBH, an off-axis jet releasing the protons at $R_{\rm acc}$, e.g., by advection, or a choked jet trapped in a quasi-static envelope.

Appendix C
Consistency of the Maximal Proton Energy

In the main text, we have parameterized the maximal proton energy $E_{p,\rm max}$. It is, however, an interesting question if $E_{p,\rm max}$ can be self-consistently described by a more realistic acceleration mechanism. A common parameterization for the acceleration rate, most appropriate for shock acceleration, is (Hillas 1984)

$$t_{\rm acc}^{-1} = \eta_{\rm acc}\, \frac{c}{R_L} \propto \frac{1}{T_{\rm cycle}} \propto \frac{B}{E} \qquad (C1)$$

with an acceleration efficiency $\eta_{\rm acc}$ typically smaller than one depending on details of the model (e.g., shock velocity,

compression rate); see Equation (7) for the definition of R_L. The maximal energy is then determined by the energy where radiative processes become faster than the acceleration.

We illustrate the acceleration rates and the processes determining $E_{p,\rm max}$ in Figure 14, assuming that (a) the acceleration and radiation zones are identical, and that (b) the interaction or escape rates limit the maximal energy (sometimes the cooling rates are used for this). With that, we can now discuss the model-dependent implications for the acceleration efficiency for the shown examples by comparing the $E_{p,\rm max}$ obtained using Equation (C1) (arrows in Figure 14) with the assumptions for $E_{p,\rm max}$ in the main text (gray-shaded areas in Figure 14):

M-X: The required acceleration efficiency is very low $\eta_{\rm acc} < 0.01$. The maximal energy will be likely determined by photohadronic interactions with the OUV target (at the BB peak). Therefore, it is plausible that acceleration and radiation zones are identical (e.g., outflow) or at a similar radius (e.g., off-axis jet), with only mild requirements for the acceleration.

M-OUV: The required acceleration efficiency for the chosen value of B is very large $\eta_{\rm acc} > 100$ if the acceleration and radiation zones are identical. This means that the acceleration must happen in a zone with stronger magnetic fields, which is also potentially more compact (unless a different mechanism, such as linear acceleration, is at work); examples could be the corona or disk if high enough proton energies can be reached.

M-IR: The maximal energy matches $t_{\rm acc}^{-1}$ for $\eta_{\rm acc} \lesssim 1$, which means that the acceleration and radiation zones could be identical if the acceleration is efficient (e.g., hidden wind-like model, or outflow–cloud/circumburst material interactions); this does not exclude that the acceleration zone could be more compact with stronger magnetic fields (e.g., an off-axis jet).

Note that there are other constraints on the acceleration region. For example, for shock acceleration triggered by the outflow, the shocks should not be radiation-mediated (which suppresses particle acceleration); see, e.g., Murase et al. (2011). The Thomson optical depth for outflow velocity v can be
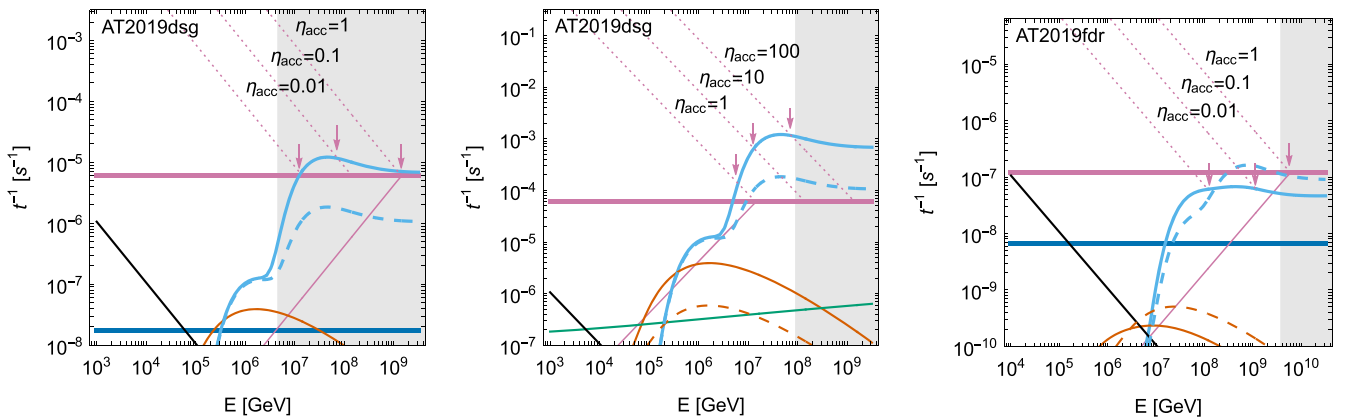

Figure 14. Acceleration rates (dotted lines) for models M-X, M-OUV, and M-IR and for different values of the acceleration efficiency, $\eta_{\rm acc}$, are shown in the left, middle, and right panels, respectively, assuming that the acceleration and radiation zones are identical. The other curves are the same as the corresponding ones in Figures 3, 6, and 9. The maximal proton energies for different $\eta_{\rm acc}$ at the BB peak time are marked by arrows, assuming that the fastest interaction or escape rate limits the maximal proton energy. Re-call that our model assumptions for $E_{p,\rm max}$ are given by the gray-shaded areas.

estimated as

$$\tau_T \simeq 0.07 \left(\frac{M}{10^7\,M_\odot}\right)\left(\frac{R}{10^{15}\,\text{cm}}\right)^{-1}\left(\frac{v}{0.5\,c}\right)^{-1}, \qquad \text{(C2)}$$

which is typically much smaller than c/v_s (with the shock velocity $v_s \sim v$ of the order of the outflow velocity). However, for more compact regions, this constraint should be considered.

ORCID iDs

Walter Winter ● https://orcid.org/0000-0001-7062-0289
Cecilia Lunardini ● https://orcid.org/0000-0002-9253-1663

References

Aab, A., Abreu, P., Aglietta, M., et al. 2017, JCAP, 04, 038
Aartsen, M. G., Abbasi, R., Abdou, Y., et al. 2013, Sci, 342, 1242856
Aartsen, M. G., Ackermann, M., Adams, J., et al. 2014, ApJ, 796, 109
Aartsen, M. G., Ackermann, M., Adams, J., et al. 2017, ApJ, 843, 112
Aartsen, M. G., Abbasi, R., Abdou, Y., et al. 2018, Sci, 361, eaat1378
Aartsen, M. G., Ackermann, M., Adams, J., et al. 2020a, PhRvL, 124, 051103
Aartsen, M. G., Ackermann, M., Adams, J., et al. 2020b, PhRvL, 125, 121104
Abbasi, R., Abdou, Y., Abu-Zayyad, T., et al. 2012, Natur, 484, 351
Abbasi, R., Ackermann, M., Adams, J., et al. 2022, ApJ, 928, 50
Andreoni, I., Coughlin, M. W., Perley, D. A., et al. 2022, Natur, 612, 430
Baerwald, P., Bustamante, M., & Winter, W. 2013, ApJ, 768, 186
Baerwald, P., Hummer, S., & Winter, W. 2012, APh, 35, 508
Bartos, I., Veske, D., Kowalski, M., Marka, Z., & Marka, S. 2021, ApJ, 921, 45
Becker Tjus, J., Hörbe, M., Jaroschewski, I., et al. 2022, Physi, 4, 473
Biehl, D., Boncioli, D., Fedynitch, A., & Winter, W. 2018a, A&A, 611, A101
Biehl, D., Boncioli, D., Lunardini, C., & Winter, W. 2018b, NatSR, 8, 10828
Blaufuss, E., Kintscher, T., Lu, L., & Tung, C. F. 2019, ICRC (Madison, WI), 36, 1021
Boncioli, D., Fedynitch, A., & Winter, W. 2017, NatSR, 7, 4882
Cannizzaro, G., Wevers, T., Jonker, P. G., et al. 2021, MNRAS, 504, 792
Cendes, Y., Alexander, K. D., Berger, E., et al. 2021, ApJ, 919, 127
Chan, C.-H., Piran, T., & Krolik, J. H. 2021, ApJ, 914, 107
Dai, L., & Fang, K. 2017, MNRAS, 469, 1354
Dai, L., McKinney, J. C., & Miller, M. C. 2015, ApJL, 812, L39
Dai, L., McKinney, J. C., Roth, N., Ramirez-Ruiz, E., & Miller, M. C. 2018, ApJL, 859, L20
Daigne, F., & Mochkovitch, R. 1998, MNRAS, 296, 275
Esteban, I., Gonzalez-Garcia, M. C., Maltoni, M., Schwetz, T., & Zhou, A. 2020, JHEP, 09, 178
Fang, K., Metzger, B. D., Vurm, I., Aydi, E., & Chomiuk, L. 2020, ApJ, 904, 4
Fang, K., & Murase, K. 2018, NatPh, 14, 396
Farrar, G. R., & Gruzinov, A. 2009, ApJ, 693, 329
Farrar, G. R., & Piran, T. 2014, arXiv:1411.0704
Fiorillo, D. F. G., Van Vliet, A., Morisi, S., & Winter, W. 2021, JCAP, 07, 028
Gao, S., Fedynitch, A., Winter, W., & Pohl, M. 2019, NatAs, 3, 88
Guépin, C., Kotera, K., Barausse, E., Fang, K., & Murase, K. 2018, A&A, 616, A179
Guetta, D., Hooper, D., Alvarez-Muniz, J., Halzen, F., & Reuveni, E. 2004, APh, 20, 429
Hayasaki, K. 2021, NatAs, 5, 436
Hayasaki, K., & Yamazaki, R. 2019, ApJ, 886, 114
Heinze, J., Biehl, D., Fedynitch, A., et al. 2020, MNRAS, 498, 5990
Heinze, J., Fedynitch, A., Boncioli, D., & Winter, W. 2019, ApJ, 873, 88
Hillas, A. M. 1984, ARA&A, 22, 425
Holoien, T. W. S., Kochanek, C. S., Prieto, J. L., et al. 2016, MNRAS, 455, 2918
Hummer, S., Baerwald, P., & Winter, W. 2012, PhRvL, 108, 231101
Hummer, S., Ruger, M., Spanier, F., & Winter, W. 2010, ApJ, 721, 630
Hung, T., Gezari, S., Cenko, S. B., et al. 2018, ApJS, 238, 15
IceCube Collaboration 2019a, GCN, 25913, 1
IceCube Collaboration 2019b, GCN, 26258, 1
IceCube Collaboration 2020, GCN, 27865, 1
Keivani, A., Murase, K., Petropoulou, M., et al. 2018, ApJ, 864, 84
Kelner, S. R., Aharonian, F. A., & Bugayov, V. V. 2006, PhRvD, 74, 034018
Kochanek, C. S. 2016, MNRAS, 461, 371
Liu, R.-Y., Xi, S.-Q., & Wang, X.-Y. 2020, PhRvD, 102, 083028
Lunardini, C., & Winter, W. 2017, PhRvD, 95, 123001
Mohan, P., An, T., Zhang, Y., et al. 2022, ApJ, 927, 74
Morejon, L., Fedynitch, A., Boncioli, D., Biehl, D., & Winter, W. 2019, JCAP, 11, 007
Mucke, A., Engel, R., Rachen, J. P., Protheroe, R. J., & Stanev, T. 2000, CoPhC, 124, 290
Mummery, A. 2021, MNRAS, 504, 5144
Mummery, A., & Balbus, S. A. 2020, MNRAS, 492, 5655
Murase, K., Kimura, S. S., & Meszaros, P. 2020a, PhRvL, 125, 011101
Murase, K., Kimura, S. S., Zhang, B. T., Oikonomou, F., & Petropoulou, M. 2020b, ApJ, 902, 108
Murase, K., Thompson, T. A., Lacki, B. C., & Beacom, J. F. 2011, PhRvD, 84, 043003
Nicholl, M., Lanning, D., Ramsden, P., et al. 2022, MNRAS, 515, 5604
Oikonomou, F. 2022, ICRC (Berlin), 37, 30
Palladino, A., & Winter, W. 2018, A&A, 615, A168
Pitik, T., Tamborra, I., Angus, C. R., & Auchettl, K. 2022, ApJ, 929, 163
Ramsden, P., Lanning, D., Nicholl, M., & McGee, S. L. 2022, MNRAS, 515, 1146
Reusch, S., Stein, R., Kowalski, M., et al. 2022, PhRvL, 128, 221101
Rodrigues, X., Heinze, J., Palladino, A., van Vliet, A., & Winter, W. 2021, PhRvL, 126, 191101
Rudolph, A., Heinze, J., Fedynitch, A., & Winter, W. 2020, ApJ, 893, 72
Senno, N., Murase, K., & Meszaros, P. 2017, ApJ, 838, 3
Shankar, F., Weinberg, D. H., & Miralda-Escude, J. 2009, ApJ, 690, 20
Stein, R. 2020, ICRC (Madison, WI), 36, 1016
Stein, R. 2021a, PhD thesis, Humboldt Univ. of Berlin
Stein, R., van Velzen, S., Kowalski, M., et al. 2021b, NatAs, 5, 510
Stone, N. C., & Metzger, B. D. 2016, MNRAS, 455, 859
Strotjohann, N. L., Kowalski, M., & Franckowiak, A. 2019, A&A, 622, L9
Tanikawa, A., Giersz, M., & Sedda, M. A. 2022, MNRAS, 515, 4038
van Velzen, S. 2018, ApJ, 852, 72
van Velzen, S., Mendez, A. J., Krolik, J. H., & Gorjian, V. 2016, ApJ, 829, 19
van Velzen, S., Stein, R., Gilfanov, M., et al. 2021a, arXiv:2111.09391
van Velzen, S., Gezari, S., Hammerstein, E., et al. 2021b, ApJ, 908, 4
Wang, X.-Y., & Liu, R.-Y. 2016, PhRvD, 93, 083005
Wang, X.-Y., Liu, R.-Y., Dai, Z.-G., & Cheng, K. S. 2011, PhRvD, 84, 081301
Wen, S., Jonker, P. G., Stone, N. C., Zabludoff, A. I., & Psaltis, D. 2020, ApJ, 897, 80
Winter, W., & Lunardini, C. 2021, NatAs, 5, 472
Winter, W., & Lunardini, C. 2022, ICRC (Berlin), 37, 997
Wu, H.-J., Mou, G.-B., Wang, K., Wang, W., & Li, Z. 2022, MNRAS, 514, 4406
Zhang, B. T., Murase, K., Oikonomou, F., & Li, Z. 2017, PhRvD, 96, 063007
Zheng, J.-H., Liu, R.-Y., & Wang, X.-Y. 2022, arXiv:2209.11005